# SEARCH FOR METASTABILITY OF 2S MUONIC NEON

---

A Dissertation

Presented to

The Faculty of the Department of Physics

The College of William and Mary in Virginia

In Partial Fulfillment

of the Requirements for the Degree of

Doctor of Philosophy

---

by

Bernhard Wilhelm Bach

1995

APPROVAL SHEET

This dissertation is submitted in partial fulfillment of the requirements for the degree of

Doctor of Philosophy

Bernhard Wilhelm Bach

Approved, June 1995

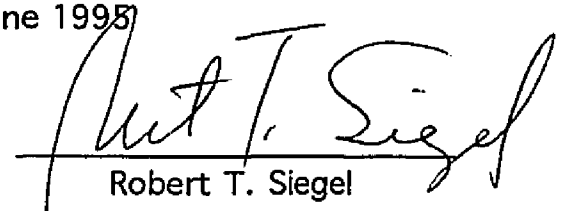

Robert T. Siegel

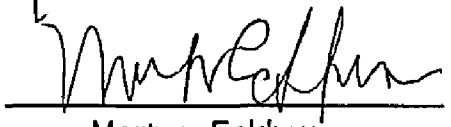

Morton Eckhause

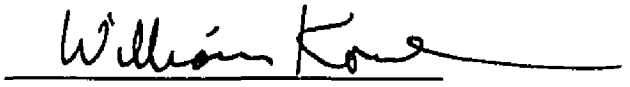

William Kossler

Marc Sher

David Abbott
Continuous Electron Beam Accelerator Facility
Newport News, Virginia

# DEDICATION

To my parents Bernhard and JoHanna, for being both mentors and friends, and for their unfailing support and encouragement of all my endeavors.

To Renée Sentilles for all her love and support, I wouldn't have made it without her help.

TABLE OF CONTENTS

ACKNOWLEDGMENTS.....vi

LIST OF TABLES.....viii

LIST OF FIGURES.....x

ABSTRACT.....xii

Page

CHAPTER 1. INTRODUCTON.....2

CHAPTER 2. THEORY.....4

A. Mesic Atom Formation.....4

B. The Cascade.....5

C. The Muonic 2S-State.....8

D. Population Of The 2S-State.....13

E. Two Photon Transitions.....15

CHAPTER 3. DISCRIPTION OF THE EXPERIMENT.....20

A. The Facilities.....20

B. The Trap.....21

C. The Cyclotron Field.....24

D. The Vaccum System.....27

E. Detectors.....28

F. Trap Tuning.....29

G. Electronics Logic and Data Acquisition.....30

CHAPTER. 4 DATA ANALYSIS.....36
A. Software.....36
B. Calibration.....38
C. Detector Efficiency.....41
D. Time Slew Correction.....43
E. Analysis Of Single Photon Events (40 Torr).....46
F. Analysis Of Two Photon Events (40 Torr).....55
G.Time Cuts Of Two Photon Events (400 Torr).....56
H. Background.....57
I. Energy Cuts On The E VS E Scatter Plot.....58
J. Analysis Of Two Photon Events (400 Torr).....60
K. Predicted Fraction Of Two Photon Decays.....68
CHAPTER 5. CONCLUSION.....73
APPENDIX.....74
REFERENCES.....81

# ACKNOWLEDGEMENTS

I would like to thank the many people who have contributed to the completion of this dissertation:

Dr. Robert Siegel, my advisor, for his time and help, and for teaching me important lessons along the way.

Dr. Leopold Simons, for the support he gave while I was in Switzerland, and his knowledge of muon physics.

Dr. David Abbott, for mentoring me on experimental techniques.

Dr. John Missimer, for his help, insight and great conversation.

Dr. Franz Kottmann, for being the pleasant person that he is, and his ability to quickly divine the source of an unexpected problem.

Dr. Peter Hauser, for all the time he spent on night shift, his great attitude, and his beer.

Dr. Dezsö Horvath, for his hard work, sense of humor, and peace keeping.

Dr. David Viel, for computer help and his general support.

Dr. Morton Eckhause, for reading the manuscript and for the kindness he has shown me during my stay at William and Mary.

Those bottle hugging fools and coaches in the corner: H.M.S. Marco Brown, Dr. Raju Subramanian, Dr. Alastair Neil, Col. Charles Martin and the Rev. Mike Walker.

Hildy Coleman, for being my dance partner over the last four years, and Matt Coffey for being my climbing partner. Without their help physical expression would have been nearly impossible in Williamsburg and I would have certainly shriveled down to the size of a Dean or Department Chairman.

Sergei Ananyan, who continually challenged me to keep my sense of humor.

Thomas "same page" Estes, for being himself.

Paula Perry, Sylvia Stout and Dianne Fannin, for all their help and laughter.

LIST OF TABLES


| TABLE | | Page |
|---|---|---|
| 2-1 | Transition Rates For The 2S and 2P States In Muonic Neon | 12 |
| 2-2 | Lyman and Balmer Series Branching Ratios | 14 |
| 2-3 | Two Photon Transition Rates For Muonic Neon | 17 |
| 4-1 | Experimental Conditions | 38 |
| 4-2 | Peak Positions In Channels (P&S Detector) | 39 |
| 4-3 | Peak Positions In Channels (W&M Detector) | 40 |
| 4-4 | Final Calibration | 40 |
| 4-5 | Fit To Detector Efficiency | 43 |
| 4-6 | Fit To Slew Correction | 44 |
| 4-7 | Single Events Muonic Neon X rays 40 Torr (P&S Detector) | 48 |
| 4-8 | Other Lines (P&S Detector) | 53 |
| 4-9 | Single Events Muonic Neon X rays 40 Torr (W&MDetector) | 51 |
| 4-10 | Other Lines (W&M Detector) | 52 |
| 4-11 | Relative Intensities Of The Lyman Series Of Muonic Neon | 54 |
| 4-12 | Number of Observed 207 KeV Two Photon Events At 40 Torr | 61 |
| 4-13 | Ratio of 2 Gamma Events to Compton Events | 62 |
| 4-14 | Number of Observed 207 KeV Two Photon Events At 400 Torr | 65 |
| 4-15 | Number of Observed 197 KeV Two Photon Events At 400 Torr | 66 |

4-16 Ratio of Observed 2 Gamma events to Compton events..... 66
At 400 Torr

4-17 Corrected 2 Gamma to Compton Ratios (197 KeV).....67

4-18 Ratio of 2 Gamma Events to Compton Events.....68
Background subtracted

4-19 Predicted and Observed 2S Decays.....70

4-20 Decay Ratios.....71

App.-1 Calibration Source Data.....74

LIST OF FIGURES


| TABLE | | Page |
|---|---|---|
| 2-1 | The Cascade | 7 |
| 2-2 | Energy Level Diagram for Z≥5 | 9 |
| 2-3 | Transition Rates | 11 |
| 2-4 | Two Photon Spectrum | 17 |
| 3-1 | Cyclotron Trap | 22 |
| 3-2 | Vaccum System | 28 |
| 3-3 | TAC Timing Diagram | 32 |
| 3-4 | Logic Diagram | 35 |
| 4-1 | Detector Efficiency | 42 |
| 4-2 | Evs. T for P&S at 400 Torr | 45 |
| 4-3 | E vs. T for P&S at 400 Torr Slew Corrected | 45 |
| 4-4 | M Series X-Rays of Muonic Neon (P&S Dectector) | 47 |
| 4-5 | K Series X-Rays of Muonic Neon (P&S Dectector) | 50 |
| 4-6 | M Series X-Rays of Muonic Neon (W&M Dectector) | 50 |
| 4-7 | K Series X-Rays of Muonic Neon (W&M Dectector) | 53 |
| 4-8 | E vs E Scatter Plot 40 Torr | 58 |
| 4-9 | Ediff 207 KeV | 60 |
| 4-10 | Ediff 210 KeV | 60 |
| 4-11 | Ediff 203 KeV | 61 |
| 4-12 | E vs E Scatter Plot 400 Torr | 63 |
| 4-13 | Ediff 207 KeV | 64 |
| 4-14 | Ediff 197 KeV | 65 |

App.-1 Detector Collimation.....75
App.-2 TAC timing $\mu$neon 3-2 transition.....76
App.-3 TAC timing $\mu$neon 2-1 transition.....76
App.-4 Compton free region.....77
App.-5 Background cut for 197 keV.....78
App.-6 Background cut for 197 keV.....78
App.-7 Energy P&S 400 Torr .....79
App.-8 Energy W&M 400 Torr.....80

## ABSTRACT

An experiment was performed at the Paul Scherrer Institut (PSI) to establish the conditions for the metastability of the 2S-state of muonic neon. The muonic atoms were formed by stopping negative muons in the neon-filled target chamber of the PSI cyclotron trap. A pair of intrinsic germanium detectors were used in coincidence to search for the two photon decay of the 2S-state. Both energy and time information from two photon events were written to disk for off-line analysis. Data were accumulated for neon pressures of 40 and 400 Torr. The data were then searched for evidence of two photon transitions from the 2S-state.

The germanium detectors were sensitive to the K-, L- and M-series x-ray photons (with energies between 10 and 300 keV) emitted during the cascade of the muonic neon ion. The detectors were also used alone to record single photon events of the K- and L-series x rays. The observed intensity ratios of the K-series x rays provided a lower limit on the initial population of the 2S-state.

For the pressure condition of 40 Torr of neon, the 2S population was found to be 1.75% ± .15% of the total cascade. The number of events at 40 Torr that could be attributed to two photons decays of the 2S-state was found to be 30 ± 52 corresponding to a 2S population of 3.8% ± 6.5%. At 400 Torr of neon the observed number of 2S two photon decays was 7 ± 41, placing an upper limit on the 2S population at 0.9% ± 5.1% of the total cascade. These results, to within the experimental uncertainties, can neither establish nor exclude the metastability of 2S muonic neon.

# SEARCH FOR METASTABILITY OF 2S MUONIC NEON

# CHAPTER 1

## INTRODUCTION

The production of muonic atoms fully depleted of atomic electrons is essential to studying such fundamental phenomena as quantum electrodynamic energy shifts, weak neutral current interactions, strange quark content of nuclei, exotic interactions and the measurement of the pseudoscalar coupling constant in muon capture. The 2S state of the muonic atoms is of special interest, since the metastability of the 2S state against the E1 photon transition to the ground state might allow for the observation of the M1 photon transition. The observation and measurement of the expected asymmetry of the M1 photon with respect to the muon spin would then provide evidence for the presence at low $q^2$ of weak neutral current interactions between hadrons and muons, and on the possible strange matter content of nuclei[1].

However, before such an experiment can be undertaken it is necessary to know how to reliably form the 2S state, as well as how to preserve metastability from modes of deexitation other than the radiative modes. The observation and timing of the 2S -> 1S two photon transition was looked for as direct evidence for the presence of the 2S state.

While the emission of two photons is the most probable radiative transition from the 2S state to the 1S state, it is not the most probable transition overall if there are electrons still present in the muonic atom. In that case other "faster" transitions such as Auger[2] and Ruderman transitions can deplete the 2S state population. Such transitions are the major obstacle to both the metastability of the 2S state and the observation of any of its purely radiative decay modes. The purpose of this experiment was to search for conditions under which the depopulation of the 2S state by these "faster" transitions was minimal.

# CHAPTER 2
# THEORY

## A. MESIC ATOM FORMATION

When a $\mu^-$ captured in the Coulomb field of a nucleus replaces one of the bound atomic electrons, a muonic atom is formed in a highly excited state. This capture is believed to occur primarily when the muon has a kinetic energy of 10-20 eV or less[2]. While the initial distribution among states after capture is not fully understood with respect to the angular quantum number $\ell$ or initial principal quantum number n, it is generally assumed that capture occurs initially in a high Rydberg state of the atom (n=14-30), with a statistical distribution in $\ell$. In such muonic atoms the muon, with a mass 207 times that of an electron, simply has the properties of a "super heavy" electron. Applying the Bohr model to such an atom one finds

$$r = n^2/Zm^* \qquad E = Z^2 m^*/n^2 \qquad (2.1)$$

, i.e., while the energy is directly proportional to the reduced mass m*, the orbital radius of the $n^{th}$ state is inversely proportional to the reduced mass.

The muon experiences only the electroweak interactions controlling atomic properties. From its initial high Rydberg state

the muon rapidly de-excites via a series of electromagnetic and Auger electron transitions referred to collectively as the "cascade". In gas targets such as the ones used in this experiment, the cascade time to the ground state depends on gas pressure but is generally of the order of $10^{-10}$ seconds or less. Because capture and cascade times are substantially shorter than the muon's lifetime of $2.2 \times 10^{-6}$ seconds, virtually all the muons reach the ground state in low Z atoms. Once in the ground state the muon can decay or be absorbed by the nucleus (the absorption rate from the 1S state is of the order of $6.5 \times 10^2 (Z^4)$ per second).

B. THE CASCADE

If, after the initial capture, the muon is assumed to be in an atomic state with quantum numbers $(n,\ell)$, transitions to the lower muonic energy states proceed by means of X-ray emissions, the ejection of Auger electrons or the "mixed" Ruderman transitions, the latter involving simultaneous emission of an x-ray and a bound electron. The selection rules for both the radiative and the Auger E1 processes are $\Delta\ell=\pm1$ and $\Delta m=0,\pm1$, with the probability depending on the cube of the transition energy $\Delta E^3$ for radiative processes and on $\Delta E^{-1/3}$ for Auger emissions[3]. The E1 Auger transitions ($\Delta n=1$) are the dominant transitions among the higher excited states ($n>5$), where the energy difference is small. However, the radiative electric dipole transitions begin to dominate at lower n in the cascade, where the transition energy is increased. These E1 transitions $((n,\ell)\rightarrow(n',\ell-1))$ rapidly bring the muon into the "circular"

states (states in which ($\ell$=n-1) for a given n). This is in contrast to the Auger E1 transitions, which tend to populate the suborbitals($\ell$) equally for muonic states with n>5.

The depletion of the electron cloud surrounding an atom is important, since the presence of electrons affects the muonic population of the "non-circular" states ($\ell \neq$n-1), of which the 2S is an example. The presence of an electron allows for the possibility of a 2S→2P Auger transition, which provides the greatest competition for the 2S->1S two-photon transition that is to be observed.

The use of a gas target allows for some control of the electron density surrounding a muonic atom. By lowering the pressure of the target gas the collision rate of the muonic atom with its neighbors is lowered, thus slowing the rate of the competing external Auger de-excitation of the 2S state. Analysis of the relative yields of the x-rays emitted during the cascade as a function of gas pressure provides information on the presence of electrons during the cascade[4]. It is expected that only 3% to 5% of the muons captured will cascade down into the 2S state[4].

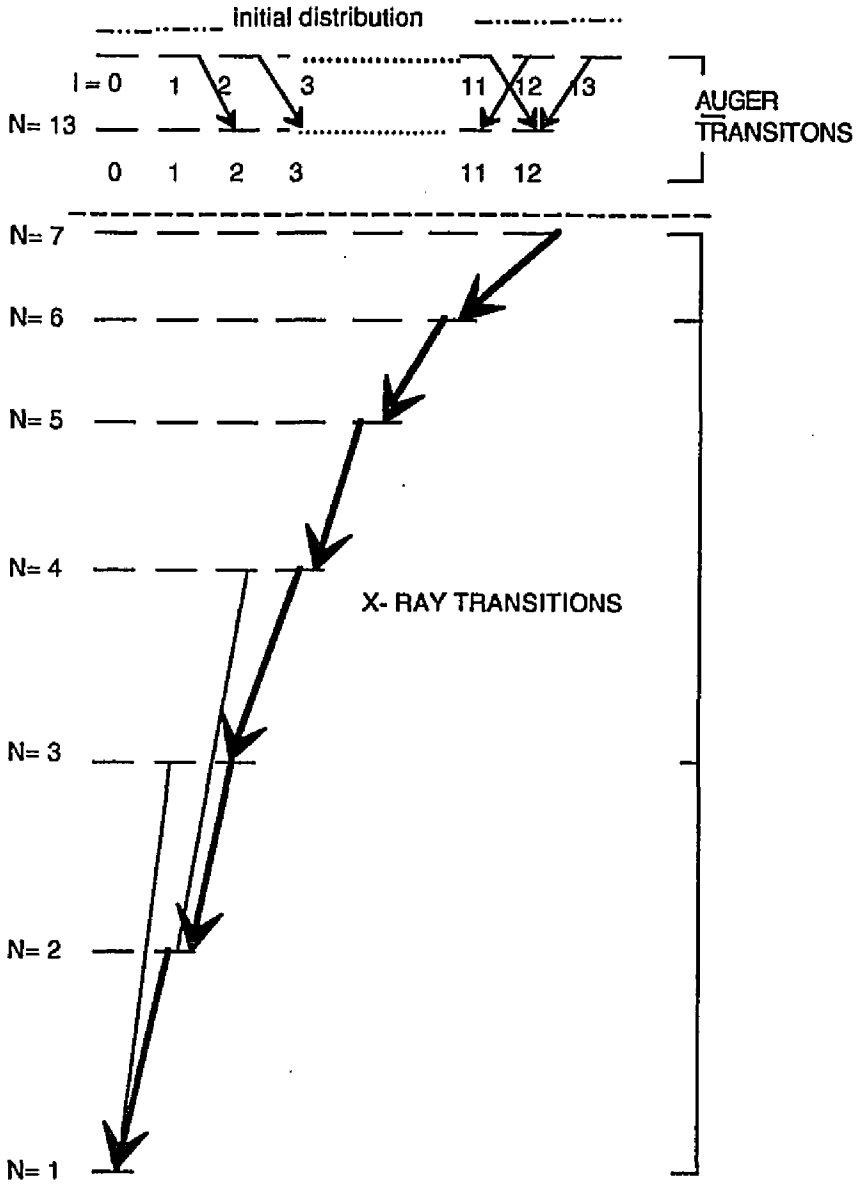


Fig. 2-1 The Cascade[5]

## C. THE MUONIC 2S STATE

The purpose of this experiment was to establish the rates and conditions under which one could reliably form muonic atoms in the 2S state. It has been pointed out that the most convenient means to detect the presence of 2S muonic atoms would be the observation of the two-photon E1 de-excitation to the ground state[6]. For nuclei with Z>5 the next three muonic states above the ground state are the $2P_{1/2}$, $2P_{3/2}$ and the $2S_{1/2}$ states. This ordering in energy is a result of the finite nuclear size effect, which raises the energy ( i.e. reduces binding) of the $2S_{1/2}$ state, but has little effect on the 2P states. With this arrangement of energy levels the $2S_{1/2}$ state has three principal modes of electromagnetic decay.

$$1)\ 2S_{1/2} \xrightarrow{M1} 1S_{1/2} + 1\gamma \qquad (2.1)$$

$$2)\ 2S_{1/2} \xrightarrow{2E1} 1S_{1/2} + 2\gamma \qquad (2.2)$$

$$3)\ 2S_{1/2} \xrightarrow{E1(m2)} 2P_{1/2}\ (2P_{3/2}) + 1\gamma \qquad (2.3)$$

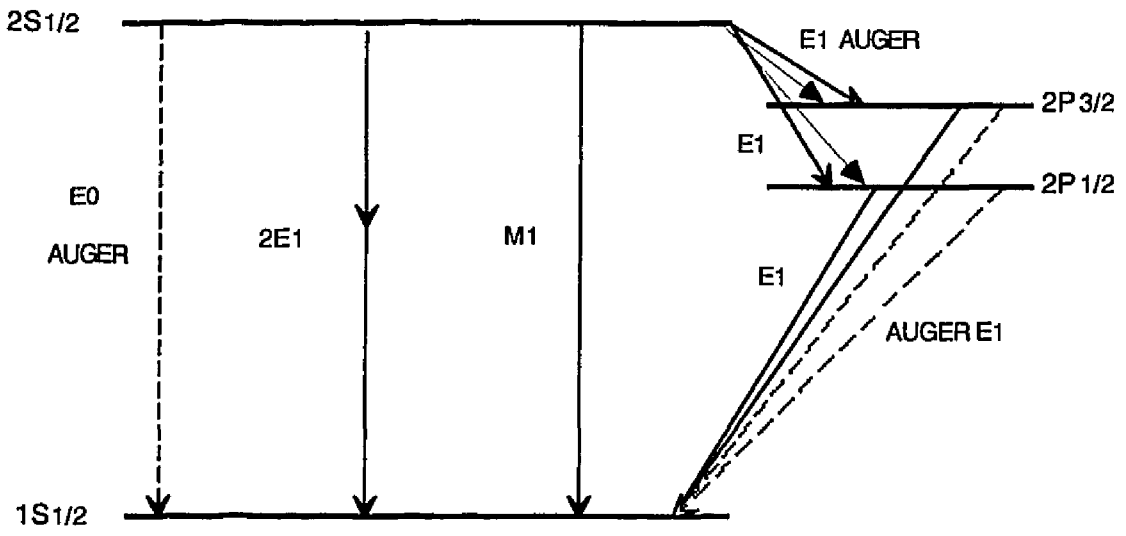


Fig. 2-2 Energy level diagram for Z≥5 [10]

The transition rates for these decay modes in hydrogenic muonic ions have been calculated by several authors[7,8] and are given below.

$$1)\ R_{2S1/2 \rightarrow 1S1/2 + 1\gamma} \approx 5\times10^{-4}\ Z^{10}\ \text{sec}^{-1} \qquad (2.4)$$

$$2)\ R_{2S1/2 \rightarrow 1S1/2 + 2\gamma} \approx 1.7\times10^{3}\ Z^{6}\ \text{sec}^{-1} \qquad (2.5)$$

While there is no general expression for the decay rate $2S_{1/2}$->2P states as a function of Z, Feinberg and Chen[7] calculate the rate to be substantially faster than that for transitions to the $1S_{1/2}$. The estimated branching ratio is expected to decrease slowly with Z, and is given by

$$R_{2s\rightarrow 1S+1\gamma} / R_{2s\rightarrow 2P1/2+1\gamma} \leq 10^{-2} \qquad (2.6)$$

for atoms with Z>17. Radiative electromagnetic transitions are not the only mode of 2S decay; there are also three possible internal

Auger transitions: $2S_{1/2}$->$2P_{1/2}$ , $2S_{1/2}$->$2P_{3/2}$ and $2S_{1/2}$->$1S_{1/2}$ , if there are electrons present. The first two of these are E1 Auger transitions, while the third is an M1, or possibly an E0 monopole transition if the initial and final states have the same spin[9]. For atoms where the 2S state lies above the 2P states in energy, the E1 Auger transitions rates have been estimated using the internal conversion coefficients for E1 nuclear transitions of equal energy[9].

$$R(2S_{1/2} \rightarrow 2P_{1/2}, 2P_{3/2}) \approx 10^{12}\ sec^{-1} \qquad (2.7)$$

The reasoning behind this approximation is that the Auger rates depend on the overlap between the muon and electron wave functions. Considering how closely bound the muon is to the nucleus, its wave function appreciably overlaps only those of the K and L shell electrons. Therefore, if there are no K and L shell electrons present in the muonic atom, these E1 auger transitions cannot contribute to the depopulation of the 2S state. There should also be no neighboring atoms so close as to provide the possibility of an external Auger transition; that is, the ejection of a electron from a neighboring atom. This leaves only the E0 2S->1S Auger rate to be considered. The transition rate for such a decay has been estimated by two authors[4,10,11] and is expected to vary slightly with Z see fig. 2-3.

$$R(2S_{1/2} \rightarrow 1S_{1/2}) \approx 3x10^{9}\ sec^{-1} \qquad (2.8)$$

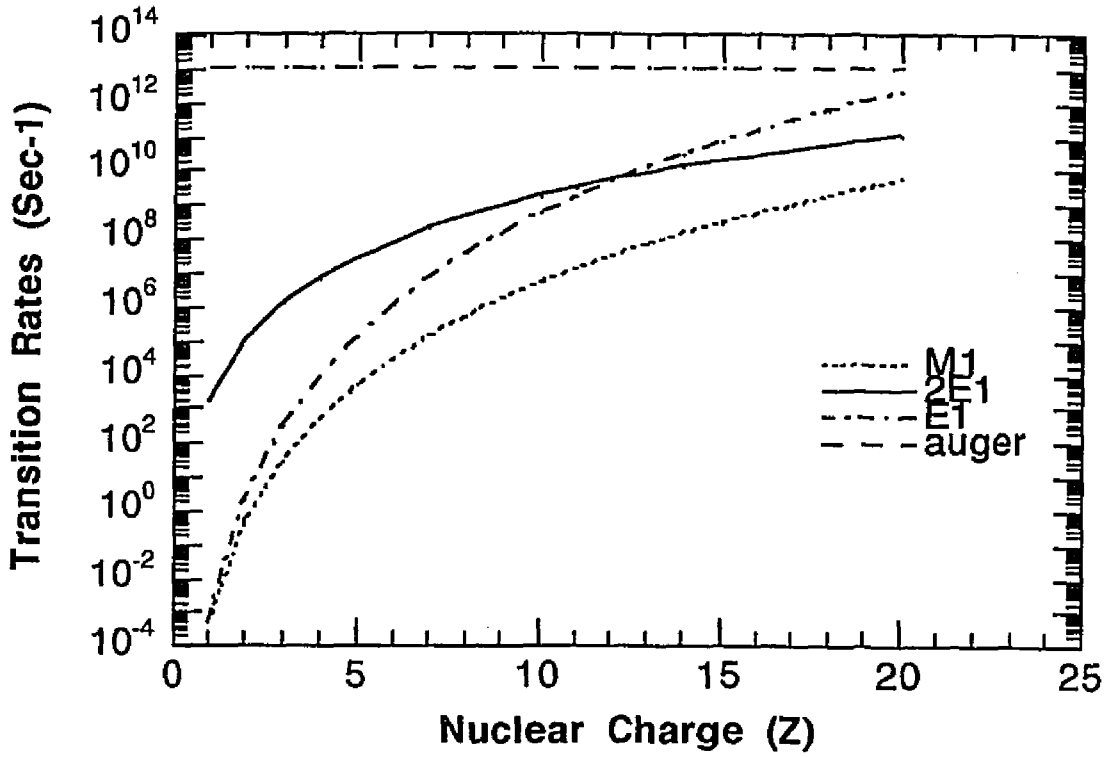


Fig. 2-3 Transition Rates

The final radiative transitions to be taken into account are the Ruderman or "mixed" transitions. If the atom is not completely stripped of electrons by the time the muon reaches the 2S state the atomic states can no longer be described by a simple muonic wave functions but by electron-muon wave functions of the form

$$|\mu^- 2S_{1/2}> | e^- n,\ell> \qquad (2.9)$$

This state can be mixed by the Coulomb interaction with the $|\mu 2P_{3/2}>$ $|e^- n',\ell'>$ electron-muon wave function where the states $|e^- n',\ell'>$ and $|e^- n,\ell>$ are of opposite parity. This mixing of states of opposite parity allows for a radiative E1 transition to the $|\mu 1S_{1/2}>$

$|e^- n',\ell'>$ state, with the photon carrying away the majority of the energy and the electron getting a small fraction. The transition rates between such "mixed" states have been estimated by Ruderman[12] to be on the order of $10^7$ to $10^9$ $sec^{-1}$ for a nuclear charge of $2 \leq Z \leq 6$. The transitions can be significant in cases where the 2S and 2P state energy difference is of the order of the electron's binding energy. For nuclear charges much larger than Z=6 the finite nuclear size effect increases the 2S-2P energy difference beyond that of the electron's binding energy, thereby reducing the rate for such "mixed" transitions. Table 2-1 exhibits rates for various 2S state processes in muonic neon.

Table2-1 Transitions rates for the 2S and 2P states in muonic neon(Z=10)

| | | |
|---|---|---|
| 2S -> 1S + 1γ (M1) | $5 \times 10^6$ | $s^{-1}$ |
| 2S -> 1S + 2γ (E1) | $2 \times 10^9$ | |
| 2S -> 2P + 1γ (E1) | $1 \times 10^9$ | |
| 2P -> 1S + 1γ (E1) | $1 \times 10^{15}$ | |
| 2S -> 1S + e (E0) | $3 \times 10^9$ | |
| 2S -> 1S + e (E1) | $1 \times 10^{12}$ | |
| 2S -> 1S + e (rearr.) | $10^7$-$10^9$ | |

## D. POPULATION OF THE 2S-STATE

In order to assess the fraction of stopped muons that form a 2S metastable muonic neon ion, it is necessary to determine the initial 2S-state population resulting from the cascade. This population can be established experimentally by measuring the yields of the K-series muonic x-rays, excluding the $K_\alpha$ ( np->1S; n >2 ).

Consider the following expression for the number of muons that enter the 1S-ground state without passing through the 2S-state:

$$N_{1s} = N_{\text{stopped-}\mu} \left[ \sum_{n\geq 2} Y(np \rightarrow 1S) + A_{1S} \right]. \qquad (2.10)$$

Y(np→1S) represents the relative intensity of the Lyman series transitions and $A_{1S}$ the sum of the relative intensities of all nonradiative transitions (Auger, Ruderman) that place a muon in the 1S state. A similar expression can be written for the number of muons that enter the 2S-state

$$N_{2s} = N_{\text{stopped-}\mu} \left[ \sum_{n\geq 3} Y(np \rightarrow 2S) + A_{2S} \right]. \qquad (2.11)$$

Here Y(np→2S) represents the relative intensity of the Balmer series transitions and $A_{2S}$ the sum of the relative intensities of all nonradiative transitions that end with the muon in the 2S-state.

The ratio of the Balmer series transition probabilities to the Lyman series transition probabilities can be found in a number of publications[13,14] and is

$$F_n(B_n/L_n) = 8 \cdot [\, n\text{-}2/n\text{-}1]^{2n-3} \cdot [n+1/n+2]^{2n+3}. \qquad (2.12)$$

This ratio is calculated and given in Table 2-2 for several selected principal quantum numbers (n) for $n \geq 3$. From table 2-2 it is clear that the value of $F_n$ is nearly constant for all quantum numbers.

Table 2-2

| $F_3$ | $F_4$ | $F_5$ | $F_6$ | $F_7$ |
|---|---|---|---|---|
| 0.1342 | 0.1418 | 0.1439 | 0.1448 | 0.1453 |

With this information we can now rewrite equation 2.11 in terms of the Lyman series intensities used to determine the observed 1S-state population

$$N_{2s} = N_{\text{stopped-}\mu} \left[ \sum_{n\geq 3} F_n \cdot Y(np \rightarrow 1S) + A_{2S} \right]. \qquad (2.13)$$

Thus the relative population of the 2S-state,

$$\varepsilon_{2S} = N_{2s} / (N_{1s} + N_{2s}) \qquad (2.14)$$

can be expressed as

$$\varepsilon_{2S}=\Big[\sum_{n\geq 3} F_n \cdot Y(np\rightarrow 1S) + A_{2S}\Big] \div \Big[\sum_{n\geq 2}(1+F_n)\cdot Y(np\rightarrow 1S) + A_{2S} + A_{1S}\Big].$$

A several experiments have measured the pressure dependent yield of various x-ray transitions in muonic noble gases[11,15]. This body of evidence suggests that below half an atmosphere a muonic noble gas ion is depleted of all electrons by the time the muon has cascaded to the n=7 state, and in the case of muonic neon that there is no electron refilling during the 200 psec of the 2S lifetime. With the muonic ion isolated from electron transfer and no atomic electrons present, the Auger transitions rates are forbidden, $A_{2S}=A_{1S}=0$, and $\varepsilon_{2S}$ can be related to the relative intensities of the K-series x-rays.

$$\varepsilon_{2S} = \Big[\sum_{n\geq 3} F_n \cdot Y(np\rightarrow 1S)\Big] \div \Big[\sum_{n\geq 2}(1+F_n)\cdot Y(np\rightarrow 1S)\Big]. \qquad (2.16)$$

## E. TWO PHOTON TRANSITIONS

Consider the $2S_{1/2}\rightarrow 1S_{1/2}$ transition in a hydrogenic atom. To first order the only allowed electromagnetic transition between these states is an M1 magnetic dipole transition. This is a result of the Wigner-Eckart theorem and reflection symmetry (parity) properties of both the states and the interaction. Because the orbital quantum numbers of both states are zero, the transition results only from the spin magnetic moments, $M_s$, acting on the spin degrees of freedom. In the non relativistic approximation the spin

and orbital components of the wave functions separate (the scalar product of the orbital components is zero), and even the M1 is not allowed. Only when one considers the relativistic corrections to the wave function is the spontaneous emission of an M1 photon allowed.

The second order interaction that describes the two-photon (2E1) process was first derived by Goppert-Meyer in 1931. Since that time more advanced mathematical methods have been applied to the problem of summing over the intermediate virtual atomic states through which the emission takes place. Currently the most accurate calculations for two photon emission are those of Klarsfeld(1969)[8], Zon and Raoport(1968)[16] and Drake(1986)[17].

If one uses the two-photon decay rate and expression given by Drake for electronic atoms, then simply substituting the mass of the muon for the mass of the electron gives the rate of the 2E1 process for the muonic atom ( $\approx 2 \cdot 10^9$ $sec^{-1}$ for muonic neon ). The single photon energy spectrum from the two-photon decay of the 2S-state is shown in Fig. 2-4, with the angular correlation between the two emitted photons described by equation 2.17.

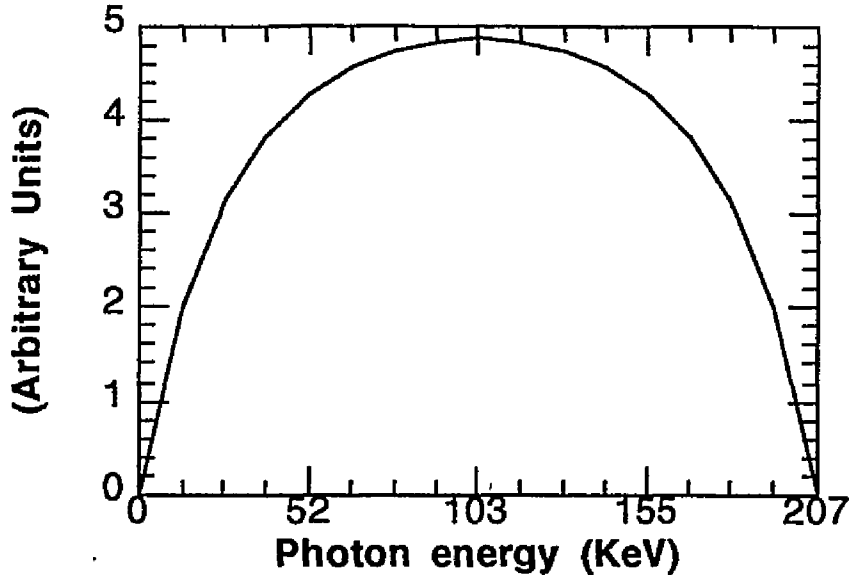


Fig. 2-4

$$W(\theta) = \text{Const} \cdot (1 + \text{Cos}^2\theta) \qquad (2.17)$$

While the 2E1 is not the only two photon process that contributes to the decay of the 2S-state, other possible transitions are suppressed. Table 2-3 lists the contributions of other multipoles to the total two-photon decay rate.

Table 2-3

Two Photon Transition Rate For Muonic Neon

| Multipole | Intermediate state | Contribution ($sec^{-1}$) |
|---|---|---|
| 2E1 | $p_{1/2}$, $p_{3/2}$ | $2 \cdot 10^{9}$ |
| E1-M1 | $p_{3/2}$ | 525 |
| 2M1 | $s_{1/2}$, $d_{3/2}$ | 28 |
| 2E2 | $d_{3/2}$,$d_{5/2}$ | 10 |
| 2M2 | $p_{3/2}$ | $8.2 \cdot 10^{-6}$ |
| E2-M1 | $d_{3/2}$ | $3.3 \cdot 10^{-7}$ |

The yield of the 2E1 channel from the 2S-state of muonic neon can be expressed

$$N_{2\gamma} = \varepsilon_{2S} \cdot \Gamma_{2\gamma} / (\Gamma_{2\gamma} + \Gamma_{E1} + \Gamma_{M1} + \Gamma_{Auger\ E1} + \Gamma_{Auger\ E0} + \Gamma_{Rearr\ e^-}). \quad (2.18)$$

The rates for these transitions have been given in table 2-1. If the muonic neon ion is fully stripped of electrons by the time the muon reaches the 2S-state then the $\Gamma_{Auger\ E1}$, $\Gamma_{Auger\ E0}$ and $\Gamma_{Rearr\ e^-}$ transitions are allowed only if the muonic ion picks up an electron during a collision with a neighboring atom. The cross section for electron transfer has been measured[18] for the case of $Ne^{+10}$ + Ne and is found to be

$$\sigma_T = 2.8 \cdot 10^{-15}\ cm^2. \quad (2.19)$$

Thus for muonic atoms with thermal velocities[11] of $v \approx 10^5$ cm/sec the electron refilling rate, $\Gamma_{Ref}$, can be calculated and substituted for the Auger and rearrangement transition rates in equation 2.18

$$\Gamma_{Ref} = n \cdot \sigma_T \cdot v. \quad (2.20)$$

Equation 2.20 combined with the ideal gas law (PV = nRT) gives

$$\Gamma_{Ref} = v \cdot \sigma_T / (R \cdot T) \approx 10^{10} \cdot P \quad (2.21)$$

where P, the pressure, is measured in atmospheres. Now expression

$$N_{2\gamma} = \varepsilon_{2S} \cdot \Gamma_{2\gamma} / (\Gamma_{2\gamma} + \Gamma_{E1} + \Gamma_{M1} + \Gamma_{Ref}). \qquad (2.22)$$

Substituting in the rates from Table 2-1 and equation 2.21 one gets

$$N_{2\gamma} = \varepsilon_{2S} \cdot 2 \cdot 10^9 / ( 2 \cdot 10^9 + 10^{10} \cdot P). \qquad (2.23)$$

At pressures of 40 and 400 Torr equation 2.23 evaluates to $N_{2\gamma} = .8\varepsilon_{2S}$ and $N_{2\gamma} = .3\varepsilon_{2S}$ respectively.

# CHAPTER 3

# DESCRIPTION OF THE EXPERIMENT

## A. THE FACILITIES

This experiment was conducted using the $\pi$E5 beam line of the ring cyclotron at the Paul Scherrer Institute in Villigen, Switzerland. The $\pi$E5 beam line was chosen for this experiment because it yields a copious number of low energy muons with a beam momentum of 30 MeV/c.

The ring cyclotron at the Paul Scherrer Institute generated a 50 MHz pulsed proton beam at an operating current of approximately 500 $\mu$A. This beam was then delivered to a carbon target. The proton-carbon collisions which took place in the target produced pions which were then directed down drift tubes, where some decayed in flight. The negative muons from this decay were focused and guided by a beam line ( of which $\pi$E5 was one) to the experimental bay, where the cyclotron trap and a beam separator were flanged to the end of the beam line. The beam separator was used to clean the beam of the many electrons present. This was necessary because the $\pi$E5 beam line yields approximately $10^3$-$10^4$ electrons per muon.

## B. THE CYCLOTRON TRAP

The cyclotron trap is a low field-index, superconducting, azimuthally, symmetric "cyclotron" operating in an inverse role: after radial injection into the perimeter of the confining field, a $\mu^-$ is decelerated in numerous revolutions via collisions with the molecules of the moderator gas, and then at the center of the trap it is captured into atomic orbitals[19]. The ability of the cyclotron trap to stop muons in a small volume of low pressure gas (down to a few tens of mbar) makes the present experiment feasible. It is necessary to work at such low pressures in order to prevent the refilling of the electron shell during the lifetime of the 2S state through collisions with the gas.

It was realized by L. Simons[20] that the weak focusing property of a cyclotron field could be used in conjunction with a low pressure gas moderator to decelerate charged particles and bring them to rest in a localized stop distribution. Such a small stop distribution alleviated a major obstacle in conducting experiments with muonic atoms. Previous to the development of the trap the physical dimensions of a muon stopping distribution in a low pressure gas was typically much larger than the solid angle acceptance detectors used to observe the created muonic atom. Because of its finite momentum spread, a muon beam stopped in a low pressure gas would have a stop distribution with physical dimensions measured in cubic meters, while a typical detector is only on the order of a few square centimeters in area. The resulting small solid angle of the detector

with respect to the muonic atoms led to an event rate so low that many experiments were unfeasible.

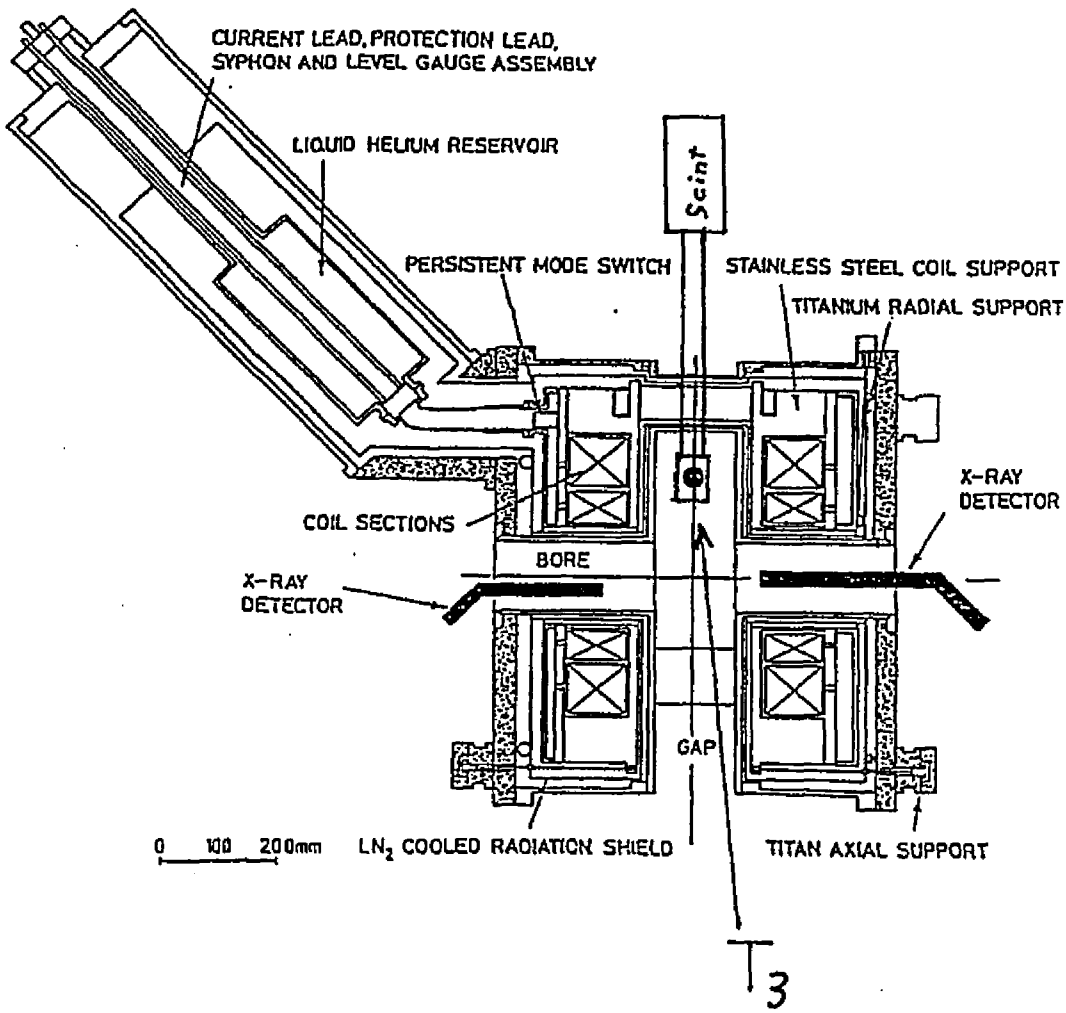


Fig. 3-1 Cyclotron Trap[20]

The cyclotron field is maintained by a pair of superconducting coils each placed in a pole face made of galvanized soft iron. Each pole face is 315 mm in radius and is separated from the other by 150 mm to form a circular dipole magnet. The superconducting coils are surrounded by a reservoir of liquid helium which is in turn

surrounded by a radiation shield cooled by liquid nitrogen. The return yoke connecting the pole faces is constructed of soft iron pillars designed to saturate at the operating field strength of 0.8 Tesla.

Access to the muon stopping region of the trap is limited by both the iron pillars and the pole faces themselves. Detector access to the stopping region is provided by two 100 mm diameter bore holes through the center of each pole face. These bore holes are 305 mm long and perpendicular to the vertical axis of the trap. Collinear with the bore holes is the center cylindrical gas chamber, which fills the 150 mm gap between the pole faces. The gas chamber is made of stainless steel and aluminum. The incoming beam of muons is introduced into the gas chamber through a 50$\mu$m thick mylar window on its circumference; this window separates the gas chamber from the iron shield that forms the entrance channel. The "entrance channel" guides the incoming muon beam from the beam pipe into the trap by suppressing the magnetic field of the trap until the muon beam reaches the injection radius of 12 cm. The entrance channel is separated from the beam pipe by another window opposite the gas chamber window, which is made of Mylar and can withstand a one atmosphere pressure differential. There are a number of other windows around the circumference of the gas chamber as well, providing access for the vacuum and gas handling systems of the experiment as well as to the $T_3$ scintillator. The $T_3$ scintillator is a beam counter which sits just beyond the entrance channel and is used to signal the data acquisition system that a muon has entered the trap.

The entire trap sits on hydraulic lifts, which are used to position the trap with respect to the beam pipe. These lifts allow the trap's attitude to be adjusted to with in a fraction of a millimeter, and are used in optimizing the number of muons injected into the trap.

## C. THE CYCLOTRON FIELD

It is well known that a charged particle moving in the presence of a magnetic field experiences the Lorentz force

$$F_L = \frac{evB}{c} . \qquad (3.1)$$

In the presence of the cylindrically symmetric field of the cyclotron trap, the Lorentz forces results in the charged particle's moving in a circular orbit, with the equation of motion given by:

$$\frac{mv^2}{r} = \frac{evB}{c} . \qquad (3.2)$$

From this expression one can define the angular frequency or cyclotron frequency $\omega$:

$$\frac{v}{r} = \frac{eB}{mc} = \omega . \qquad (3.3)$$

The cyclotron frequency is approximately constant for a typical cyclotron. This is a result of the fact that the cyclotron's field, B, is a simple dipole field, which falls off slowly with increasing radius as one approaches the edge of the magnet. This drop in field strength is on the order of a few percent and is ultimately responsible for the stability of orbits in the cyclotron.

The question of orbital stability is a major aspect in the design of an accelerator, or, in this case, a decelerator. Practically none of the muons are injected into the trap accurately enough to travel their entire path length unguided. The solution to this problem is to shape the field of the cyclotron in such away as to provide corrective steering forces for particles that deviate from the desired or "equilibrium" orbit. In a cyclotron there are two directions in which the particle can deviate from its equilibrium orbit: the radial direction and the axial(dipole axis) direction. It is in these two directions that stability must be maintained.

It can be shown[21] that in a cyclotron the deviations from the closed equilibrium path in either the radial or axial direction can be approximated by the equations of simple harmonic motion. These equations are known as the Kerst-Serber equations for the perturbed axial and radial motion and are of the form:

$$M \frac{d^2y}{dt^2} + K^2 y = 0 , \qquad (3.4)$$

where y is the deviation and $K^2$ is the restoring force per unit displacement. The Kerst-Serber equation for the perturbed axial motion of the cyclotron is given by

$$\frac{d^2z}{dt^2} + \omega^2 n z = 0 \qquad (3.5)$$

where z=0 is the mid-plane of the field where the equilibrium orbit lies and there is no radial component of the field, and n is the field index, defined as

$$n = -\frac{dB}{dr}\frac{r}{B} \qquad (3.6)$$

For the case of $n > 0$ the solutions to the axial motion are sinusoidal, the beam oscillates about z=0, the mid-plane. The equation for the radial perturbed motion is of the form

$$\frac{d^2x}{dt^2} + \omega^2 (1 - n) x = 0 \qquad (3.7)$$

where x is the radial deviation from the equilibrium orbit which is circular. As in the axial case, this equation supports sinusoidal solutions but for the condition $n < 1$. Thus, for the beam to be stable about the equilibrium orbit in both the radial and axial directions we require $0 \leq n \leq 1$. For such values of n the beam oscillates about the equilibrium orbit in what are referred to as the betatron oscillations.

These betatron oscillations determine the size of the stop distribution in the center of the trap. Detailed analysis of the oscillations was performed by L. Simons[20]. He showed that the radial extension of the stop distribution was just the width of the initial beam, while the axial width could be expected to be a factor of two greater than the axial width of the initial beam. However, the betatron oscillations must be excited in such a fashion that the

beam passes only once through the plastic foil moderator. The moderator is used to decrease the beam momentum down to the acceptance momentum of the "first" equilibrium orbit. If the beam were to pass through the moderator more than once this would lead to non-circular orbits and increase the size of the muon stop distribution. In order to avoid this, the beam must be injected at a slight angle of 110 mRad to the mid-plane of the trap. Unfortunately this injection scheme leads to a slight increase in the width of the stop distribution. The beam momentum is degraded further due to collisions with the gas that fills the target chamber. It is this gradually loss of energy in the target gas combined with the weak focusing of the magnet that guides the beam through a series of equilibrium orbits that lead to the center of the trap.

## D. THE VACUUM SYSTEM

The center of the cyclotron was evacuated using two staged pumps: a roughing pump and a turbo-molecular pump, both attached to the target chamber through a large diameter tube. The turbo pump could be isolated from the target chamber and roughing pump by means of two separate valves(see diagram). Located between the target chamber and turbo pump was a vacuum gauge accurate to $10^{-9}$ Torr, a vent valve and a lead-in from the gas handling system. The gas of interest was introduced into the target chamber through this lead-in, which was equipped with a pressure gauge and needle valve.

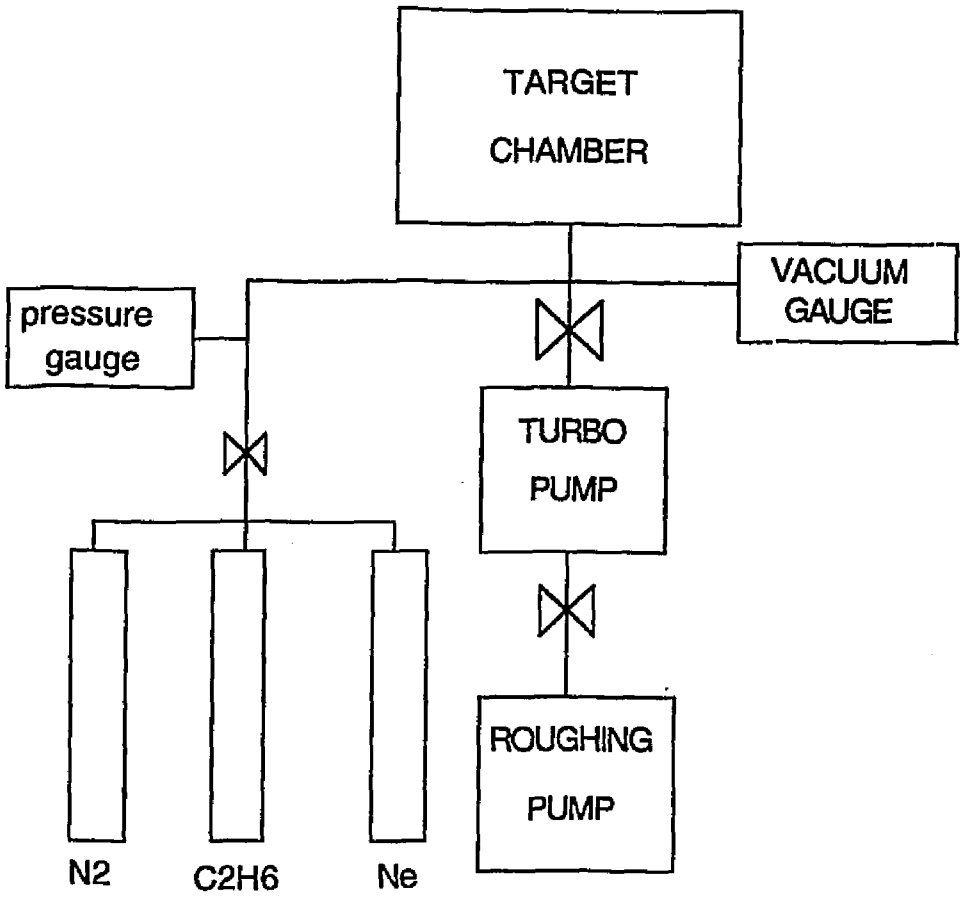


Fig 3-2 Vacuum system

## E. DETECTORS

Two identical detectors, denoted W&M and P&S, were used during this experiment. Both of the detectors were planar high purity or intrinsic germanium detectors, and were used to observe the x-ray transitions of the target gas. The W&M detector had an active region 2000 $mm^2$ by 13mm thick (corresponding to a peak efficiency at ≈ 50 kev) which was connected to a resistive feedback preamplifier to give an energy resolution of 640 eV at 122 keV. P&S is identical to W&M but with a energy resolution of 610 eV at 122 keV.

Each detector was fitted with a plastic sleeve that allowed it to be inserted into the bore holes of the trap to form a vacuum tight seal. The detectors were mounted from opposite sides of the trap so as to face each other across the target chamber of the trap. In order to optimize the signal to noise ratio, and keep the pileup rate to a minimum, it was necessary to limit each detector's view to the muon stop region rather than the whole interior of the trap. This was accomplished with the use of brass collimators, and by adjusting the distance between the detector and the center of the trap. The collimation is formed by two brass rings, each 18mm thick with a 50mm hole in the center, which are placed in front of the detectors, see Fig. App-1. The optimal distance between detector and trap center was determined experimentally during the tuning of the trap.

## F. TRAP TUNING

Before attempting to collect data the trap was first tuned to maximize the number of muons stopped in the center of the trap. The tuning process consisted of filling the gas chamber with $N_2$ to a pressure that would provide the stopping power equivalent to that of the target gas at the pressure to be used in the actual experiment. Nitrogen was the gas of choice for this procedure because it had been used for tuning purposes in previous runs and so offered a standard by which to judge the stopping distribution.

The W&M detector was inserted into the bore holes at a distance of 80mm from the center of the trap. The muon beam was then

injected into the trap and μN x-ray rates were measured. The trap was then adjusted vertically and horizontally, and changes were also made to the beam momentum spread, angle of injection and detector position as well. All of this was done with the intention of maximizing the μN x-ray rate and thereby the count rate for all subsequent experiments.

The muon beam injected into the trap is actually an electron beam with a few muons- the $e^-/\mu^-$ ratio is $10^3$ -$10^4$ (P. Hauser, private communication.) Because of this fact, a crossed electric magnetic field separator is placed between the trap and the beam pipe to clean the beam of electrons. While most of the electrons can be removed by the separator and by use of an RF gate, there are still a large number of electrons entering the trap compared to muons. These electrons, along with off-axis muons, generate a background signal with a rate large enough to overwhelm the preamps of the detectors. This is remedied by further collimation of the beam; the unwanted portion of the beam is stopped by aluminum baffles that cover the section of the trap's entrance channel where the unwanted beam originates. Ideally, this leaves only the muons that produce a uniform stopping distribution in the trap's center. The typical singles counting rate for each detector was on the order of $10^3$ μN x-rays $sec^{-1}$.

## G. ELECTRONIC LOGIC AND DATA ACQUISITION

To ensure the proper timing of each event, the output signals from the detectors and the $T_3$ scintillator were shaped by a series of

fast electronic modules before being recorded by the computer. A total of four different signals were used to "define" the coincident events recorded by the data acquisition system.

The time between a muon passing through the $T_3$ scintillator and the detection of a muonic x-ray in the germanium detectors was measured using the logic shown in figure 3-3. The signal from $T_3$ passed through a constant fraction discriminator (CFD) and then into a gate and delay generator to create the $T_3$ gate and the $T_3$ delay. A gate was also generated from the 50 MHz RF signal of the cyclotron. The RF gate discriminated between the arrival of electrons and muons at the trap. This discrimination is possible because the heavier muon has a lower velocity than that of an electron for a given momentum, causing the muons to arrive between the 50 MHz electron pulses. The RF gate in coincidence with a $T_3$ gate formed the $T_3$*RF signal, indicating the presence of a muon in the trap. It is also the $T_3$*RF signal that is used in coincidence with detector timing signals to identify only those events which correspond to muonic x-rays.

The timing signals for each detector were obtained by passing the detector outputs through a timing filter amplifier (TFA) and CFD, and then delayed by approximately 200 nsec to ensure that they would be later than the start of the $T_3$*RF gate. The time at which a detector event was coincident with the $T_3$*RF gate was measured in a time to amplitude converter (TAC) relative to the end of the $T_3$ gate, which was 3μsec wide. The coincident $T_3$*RF*P&S(W&M) signal was then fed to a gate generator whose TTL output pulse was stretched for the purpose of defining a gate for the energy signal

from each detector. The $T_3$*RF*P&S(W&M) signal also functioned as the end marker for the multi-channel analyzer (MCA) that was used during this experiment.

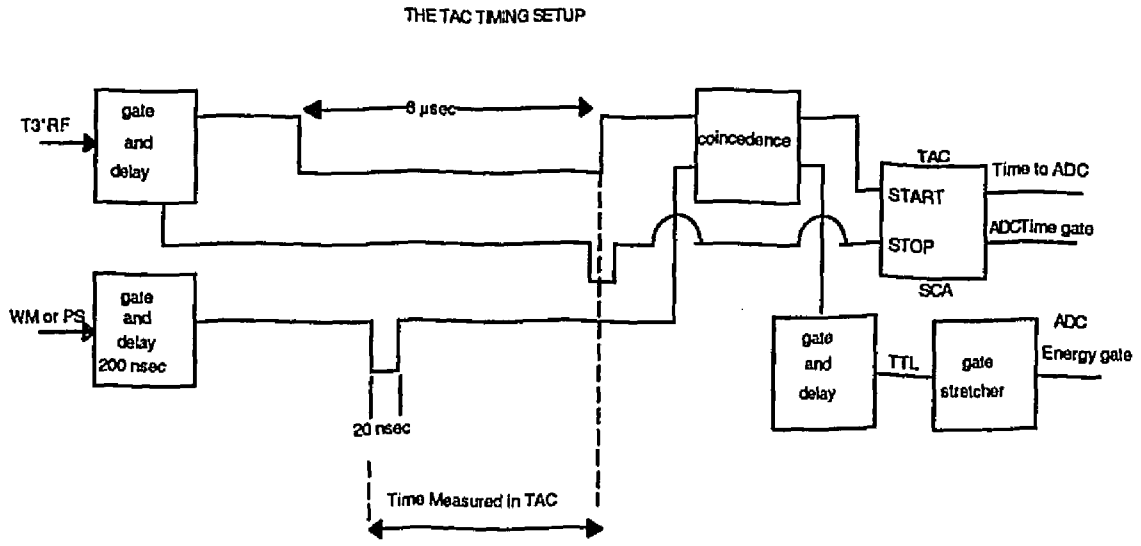


Fig. 3-3 TAC Timing Diagram

A quad input 13 bit ADC (Ortec 413A) was used to digitize the TAC and energy information for each detector. The ADC accepts five separate gates, four of which are specific to the individual inputs while the fifth gate is a master gate which can "allow" or "inhibit" conversion of all four inputs. This master gate was used to "allow" digitization of only those events coincident between the two detectors.

Table 3-1

| *inputs* | *input signal from* | *gate signal from* |
|---|---|---|
| *1* | *P&S TAC* | *SCA output from TAC(P&S)* |
| *2* | *P&S energy* | *coin. .T3*RF*P&S* |
| *3* | *W&M TAC* | *SCA output from TAC(W&M)* |
| *4* | *W&M energy* | *coin.T3*RF*W&M* |

The logic of the master gate follows. Because of the high counting rates and large baseline noise in the detector signals, the best timing between the detectors outputs was about 150 nsec FWHM. In order not to lose any true coincident events due to this "loose" timing a "wide" coincidence was set up between the detectors. The $T_3$*RF*W&M and $T_3$*RF*P&S signals were fed into gate stretchers to create two gates approximately 500 nsec in width. These 500 nsec gates were then sent to a AND/OR logic gate whose output, in coincidence with the 10 μsec wide $T_3$*RF gate, was sent to a delay and gate stretcher and widened to 1μsec for the purpose of defining the master gate.

In parallel to the one described above there was a second timing circuit which used a LeCroy 4208 time to digital converter (TDC) to measure the relative timing between the two detectors. The TDC was operated in common start mode with the TDC start being generated from a $T_3$*RF*P&S*W&M signal. The individual TDC stop signals for each detector consisted of the $T_3$*RF*P&S(W&M) gate in coincidence with a second detector timing signal which had passed through an upper level discriminator (ULD) and gate generator. The TDC LAM, TDC CLEAR and TDC START signals were all generated from the coincidence of the 500 nsec $T_3$*RF*P&S, $T_3$*RF*W&M gates with the 10 μsec $T_3$*RF gate, which defined the master gate. The TDC LAM used the TTL output from a gate generator that had received the coincidence signal, while the stretched NIM output of the gate was used to trigger a Flip-Flop that controlled the TDC CLEAR and TDC START signals (see FIG. 3-4 ).

Each detector's preamp output was sent to a Tennelc spectroscopy amplifier for shaping and amplification. The outputs from these amplifiers along with the TAC outputs were then passed to the ADC's for simultaneous recording by the Macintosh and VAX.

The Macintosh and Vax computers controlled separate CAMAC crates that contained a crate controller and identical Ortec 413A quad ADCs, LeCroy 4208 TDCs and LeCroy 4434 scalers. Kmax, a commercially available data acquisition program for the Macintosh, was used to control the CAMAC crate, sort events, and create 1D, 2D and 3D histograms of the collected data. The VAX used a PSI "home grown" data acquisition program called HIX, which performed the same functions as Kmax. The MCA contained two 2000 channel ADC units capable of recording the 1D energy spectra from each detector. These spectra were then saved to floppy disk.

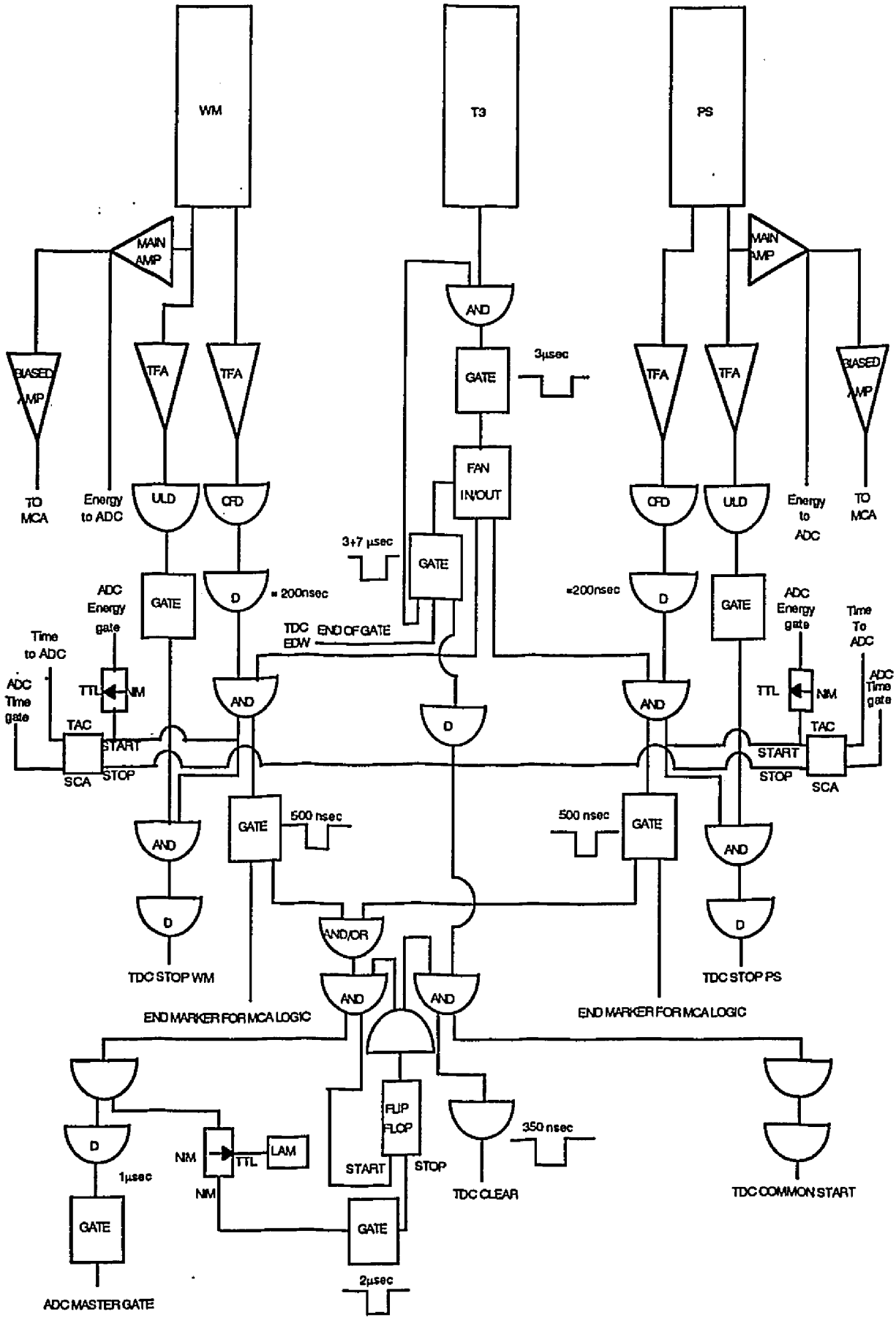
WM
T3
PS
MAIN AMP
MAIN AMP
BIASED AMP
TFA
TFA
TFA
TFA
BIASED AMP
AND
GATE
3μsec
FAN IN/OUT
TO MCA
Energy to ADC
ULD
CFD
CFD
ULD
Energy to ADC
TO MCA
3+7 μsec
GATE
ADC Energy gate
GATE
D
≈200nsec
≈200nsec
D
GATE
ADC Energy gate
Time To ADC
TDC EDW
END OF GATE
Time to ADC
ADC Time gate
TTL
NIM
AND
AND
D
TTL
NIM
ADC Time gate
TAC
START
STOP
SCA
SCA
STOP
START
TAC
AND
GATE
500 nsec
500 nsec
GATE
AND
D
AND/OR
D
TDC STOP WM
AND
AND
TDC STOP PS
END MARKER FOR MCA LOGIC
END MARKER FOR MCA LOGIC
D
1μsec
NIM
TTL
LAM
NIM
FLIP FLOP
START
STOP
350 nsec
TDC CLEAR
TDC COMMON START
GATE
GATE
2μsec
ADC MASTER GATE

# CHAPTER 4

# DATA ANALYSIS

## A. SOFTWARE

The analysis was accomplished with two software programs, Kmax[22] and FIT[23]. The Kmax program used to record the data also has a data analysis capability. For a defined region Kmax can give the centroid position, full width half maximum (FWHM), peak sum and peak area (sum minus background). Kmax also has a built in scripting language, allowing one mathematically to manipulate the data before sorting it into histograms. This feature was used to make the time slewing and efficiency corrections to the data.

FIT is a fast interactive program for the fitting of various kinds of data, simple lists of numbers (x), or files containing pairs of numbers (x,y), FIT accepts the 1D spectra generated by ADCs and TDCs, and the errors associated with such data. For our application the fitting of x-ray spectra, the program made use of the fast Marquard fitting algorithm. This algorithm is particularly efficient at optimizing the parameters of a given fitting function so as to generate a minimum chi-square.

There are 32 predefined functions in FIT (they include constant, linear, Gaussian, Fermi, Sasamoto-Gaussian, etc.,) and room for

seven user defined or custom functions, all of which can be used in combination to fit a complex spectrum. Each function has a number of parameters that are varied to fit the spectra. The program evaluates these parameters and places the results in a fit-array. This array is compared with the data-array and the value of chi-square is calculated. FIT uses routines taken from Bevington[24] to calculate the error in the given value of the parameter. Once the errors have been calculated, FIT can then integrate the fit-array over the fitting interval and the peak sum and peak area are found along with their associated errors.

In its current form FIT has a number of constraints; the maximum length of the fitting interval is 8192 data points, the maximum number of functions in a fit is 200 and the maximum number of free variables is 100. The size of the function cache is another constraint in that the product of the number of channels and the number of functions in a fit cannot exceed 2 $x10^5$, which is to say one could fit up to 200 functions to 1000 data points, or 25 functions to 8192 data points. Due to these limitations it was necessary to fit the energy histograms in three seperate sections, see section 4 E.

The Kmax recorded data are composed of six fields, three per detector: the energy, TAC time and TDC time for each event. The data runs were made at pressures of 40 and 400 Torr of neon; both single and coincident data were recorded for the 40 Torr condition, see table 4-1. Data were accumulated in record event format files that were titled and numbered sequentially. Periodically during the evening a run was halted and the target chamber evacuated. The

was done to minimize the contamination of the neon from out gassing of the trap and any slow leaks in the gas handling system.

Table 4-1

Experimental Conditions

40 Torr neon coincidence

40 Torr neon singles

400 Torr neon coincidence

B. CALIBRATION

There were two energy calibrations performed for each detector, one for neon at 40 Torr runs and one for neon at 400 Torr runs. Calibrated sources of the radionuclides, CO-57, AM-241 and Bi-207, were installed in the trap during the tuning phase. The known emission lines from these sources provided a reference by which to set the amplifier gain, shaping time and pole-zero controls so as to optimize the energy resolution for each detector. Table App.-1 lists half lives, photon energy and emission probabilities for selected emission lines from the three sources.

During the actual data runs a "working" calibration of the spectra was made using the calibration option provided by Kmax. For the analysis it was necessary to have a calibration more accurate than the "working" calibration. The spectra of muonic neon was fit with Gaussian peak shapes using FIT. The energy, position, FWHM, and amplitude are listed in Table 4-2 and 4-3. A linear function was fit

to the position of the neon lines using the least squares method. The resulting calibrations are given in Table 4-4.

Table 4-2

| P&S | 400 Torr Neon | | | 40 Torr Neon | | |
|---|---|---|---|---|---|---|
| Line I.D. Energy | Channel Position | Channel FWHM | AMP. | Channel Position | Channel FWHM | AMP. |
| μne 3-1 246.17 keV | 2497.5±.3 | 9.8±.6 | 31±2 | 2498.3±.6 | 9±1 | 12±1 |
| μne 2-1 207.22 keV | 2101.5±.04 | 10.26±.08 | 953±11 | 2102.8±.09 | 10.3±.2 | 195±5 |
| F-19 γ-ray 197.15 keV | 2000.7±.2 | 15.97±.54 | 56±2 | | | |
| μne 3-2 38.947 keV | 391.07±.02 | 7.53±.04 | 2647±23 | 391.44±.05 | 7.92±.09 | 531±10 |
| μne 4-3 13.624 keV | 133.29±.02 | 7.73±.05 | 2054±20 | 133.37±.06 | 8.3±1 | 396±9 |

Table 4-3

| W&M | 400 Torr Neon | | | 40 Torr Neon | | |
|---|---|---|---|---|---|---|
| Line I.D. Energy | Channel Position | Channel FWHM | AMP. | Channel Position | Channel FWHM | AMP. |
| μne 3-1 246.17 keV | 3363.9±.7 | 13±2 | 14±2 | 3364.8±.8 | 25±2 | 8.7±.8 |
| μne 2-1 207.22 keV | 2831.4±.07 | 16.15±.13 | 511±7 | 2833.8±.16 | 16.41±.29 | 114±3 |
| F-19 γ-ray 197.15 keV | 2688.5±.2 | 7±.5 | 38±3 | | | |
| μne 3-2 38.947 keV | 532.29±.04 | 13.15±.07 | 1444±13 | 533.62±.09 | 14.59±.16 | 335±6 |
| μne 4-3 13.624 keV | 185.97±.05 | 13.80±.09 | 1130±11 | 186.8±.1 | 14.74±.20 | 231±5 |

Table 4-4
Energy(keV) = m x Channel No. + b

| 40 Torr neon | m (keV/channel) | b (keV) |
|---|---|---|
| W&M | 0.07306 ± .00003 | 0.829 ± .032 |
| P&S | 0.09824 ± .00002 | 0.480± .028 |
| 400 Torr neon | m (keV/channel) | b (keV) |
| W&M | 0.07316 ± .00002 | 0.81 ± .038 |
| P&S | 0.09835 ± .00003 | 0.611 ± .054 |

## C. DETECTOR EFFICIENCY

Inorder to properly determine the two-photon emission rate of the 2S-state it is necessary to take into account the relative photopeak efficiencies of each detector between 10 keV and 207 keV. Prior to the experimental run the energy dependence of the photopeak efficiencies of the detectors were measured using selected emission lines from three calibrated sources: Co-57, Am-241 and Ba-133, see table App.-1. This procedure allowed the relative efficiencies to be determined up to an energy of 136.47 keV, with about a 5% accuracy. For energies greater then 136.47 keV it was necessary to rely on the Monte Carlo calculated photopeak efficiencies of Seltzer[25]. This calculation spanned an incident photon energy range from 60-400 keV and was consistent with the experimentally determined values below 136.47 keV (see Fig. 4-1).

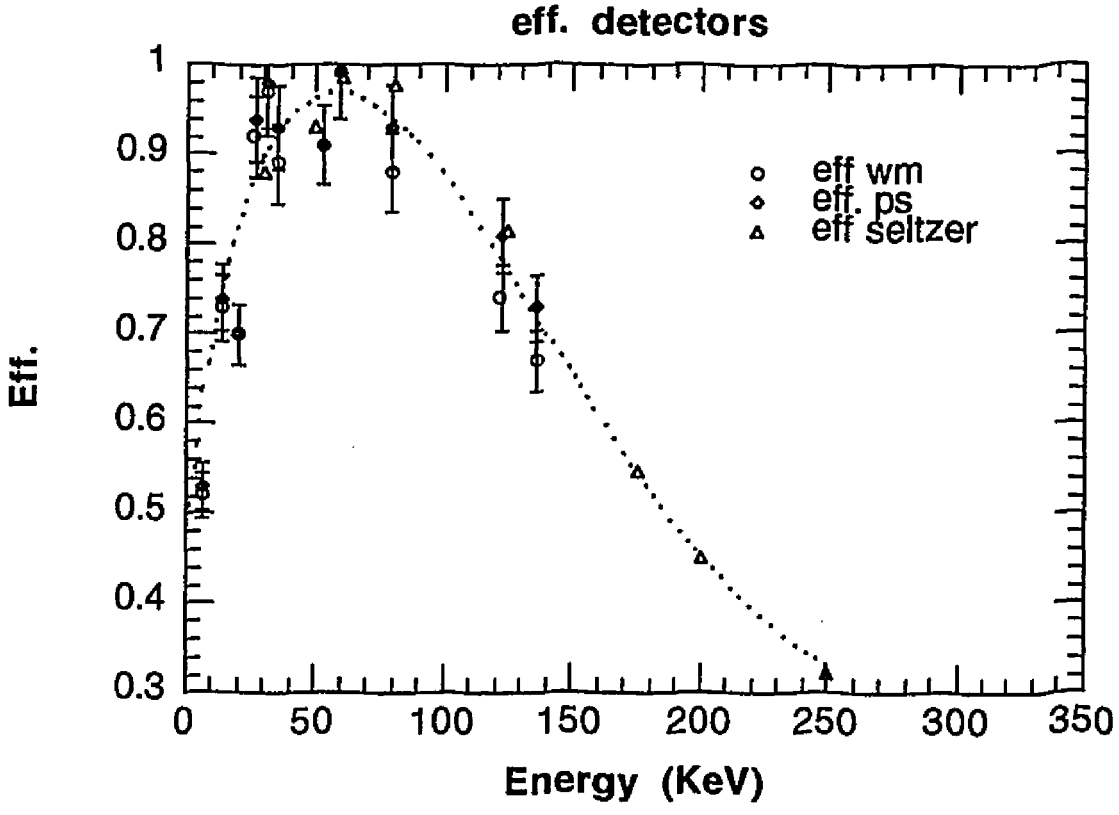


Fig. 4-1 Detector Efficiency

To interpolate between the measured values of an efficiency-calibration curve it is a common practice to fit the data points to a analytical function, typically a polynomial energy. In this case Kaleidagraph was used to fit the data to a fourth order polynomial function. The result of the least squares fit is shown below in Table 4-5.

Table 4-5

$\varepsilon(E) = M0 + M1(E) + M2(E^2) + M3(E^3) + M4(E^4)$

| | |
|---|---|
| M0 | $0.468 \pm 0.052$ |
| M1 | $0.019 \pm .002$ |
| M2 | $-0.00022 \pm 3 \cdot 10^{-5}$ |
| M3 | $8.73 \cdot 10^{-7} \pm 1.9 \cdot 10^{-7}$ |
| M4 | $-1.1 \cdot 10^{-10} \pm 3.2 \cdot 10^{-10}$ |
| $\chi^2$ | 0.977 |

D. TIME SLEW CORRECTION

Looking at the 2-D plots of energy vs. time, one notices that lower energy events are measured at later times than events of higher energy; see Fig. 4-2. This distortion is know as time slewing and results from the variation in pulse shape of signals entering the constant fraction discriminators CFD used in the timing logic. The zero crossing level of a CFD is a function of pulse height (i.e. proportional to energy) and the smaller the pulse height the later the zero crossing, see Fig App.-1 and Fig. App-2. To determine the amount of time slewing as a function of energy, Kmax was used to find the time centroid of the prompt peaks in the 1-D timing histograms for selected lines of known energies. Kalidagraph was then used to fit the position of the timing centroids to a function of the form.

$$\text{Time} = (A/\text{Energy}) + B \qquad (4.1)$$

Table 4-6 gives the results of the fit.

Table 4-6

Time(E) = A/Energy + B

| 40 Torr | A | B | $\chi^2$ |
|---|---|---|---|
| P&S | 3592 | 4313 | .995 |
| W&M | 4189 | 4346 | .976 |
| 400 Torr | A | B | $\chi^2$ |
| P&S | 1715 | 4537 | .988 |
| W&M | 2037 | 4616 | .976 |

With this functional form for the energy dependence of the timing, the slew correction can then be made by modifying the software of the replay instrument used to analyze the data. The new instrument accomplishes this correction by subtracting the value of the time from equation 4.1 minus the constant B from the time channel of the event. The constant B is only the prompt peak's offset from the time zero and need not be included in the slew correction. The new instrument is then used to create slew-corrected histograms; see example fig. 4-3.

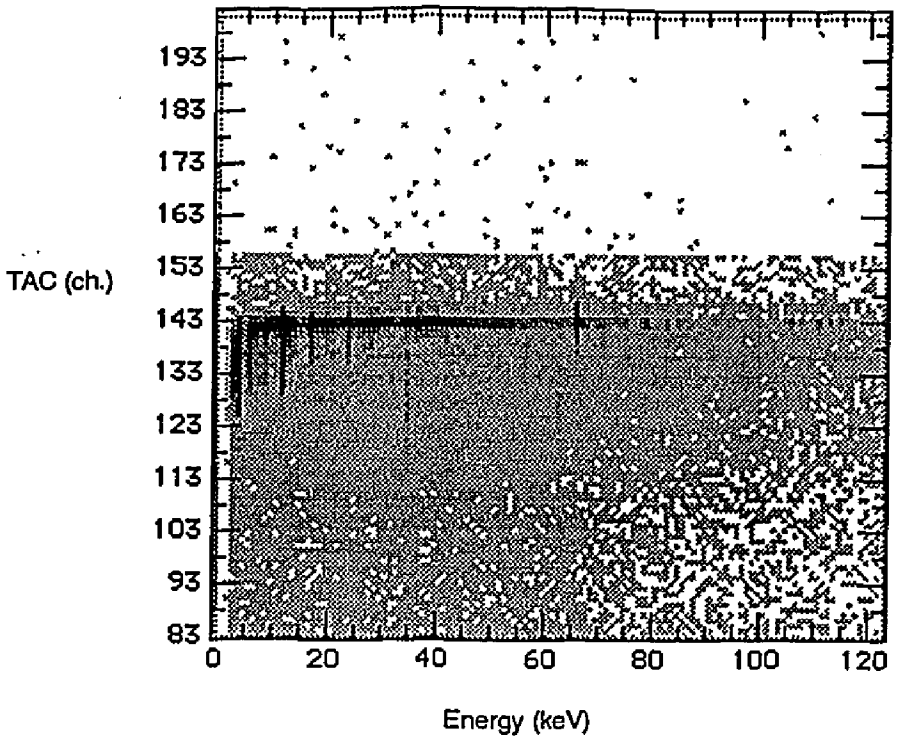


Fig. 4-2, E vs. T for P&S at 400 Torr

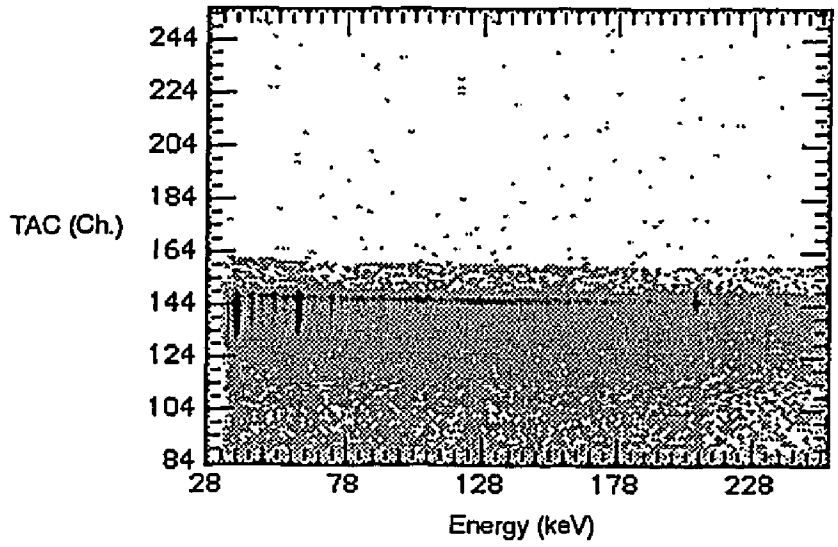


Fig.4-3, E vs. T for P&S 400 Torr Slew Corrected

## E. ANALYSIS OF SINGLE PHOTON EVENTS

For the phase of the experiment during which data was collected at 40 Torr of neon in the trap, data were accumulated in both coincidence and singles mode. Periodically, the coincidence runs were stopped and the logical condition between the detectors was changed from an AND (coincidence) to an OR gate (singles mode). For an event to be recorded in this fashion, there only needed to be a single photon registered in either of the detectors.

The data collected in these individual singles runs were saved in thirteen event files. The Neon Singles event files were later replayed and the data summed into histograms for analysis. Energy spectra of the single photon events occurring in each detector were then fitted using FIT. After corrections had been made for relative detector efficiencies the results of the fit could then be used to calculate the intensity ratios of the muonic neon x-rays. These ratios give an estimate of what fraction of muons end in the 2S-state as a result of the cascade.

The energy spectra from both detectors were sorted into 8192 channel histograms and fitted in both channel numbers and in the calibrated energy scale given for 40 Torr of neon-see Table. 4-6. To expedite the fitting procedure, the 8192 channel histograms were fitted in three separate sections, each section being centered on an x-ray series of muonic neon. The first section fit was centered on the K series (n-1) x-rays and covered an energy range from 190 keV to 380 keV. The second section consisted of the K series (n-2) x-rays and ranged from 35 keV to 70 keV. The gap from 70 keV to 190

keV is temporally ignored here as it contains no muonic neon x-rays, only x-rays generated from muons stopped in the surrounding trap material and gamma rays resulting from muon nuclear capture. Section three contains the M series (n→3) x-rays and extends from 10 keV to 38 keV. Table 4-7 lists the fitted emission lines observed in the P&S detector. It is worth noting that the higher K series transitions n>4 were very weak, and in order to fit them it was occasionally necessary to fix the parameters of a neighboring stronger peak. For each section of the spectrum the emission lines were fit with three-parameter (position, FWHM, amplitude) Gaussian peaks and a linear background was assumed. Both the peaks and the background were fit using the least-squares method, see Fig. 4-4 thru 4-7.

Fig. 4-7

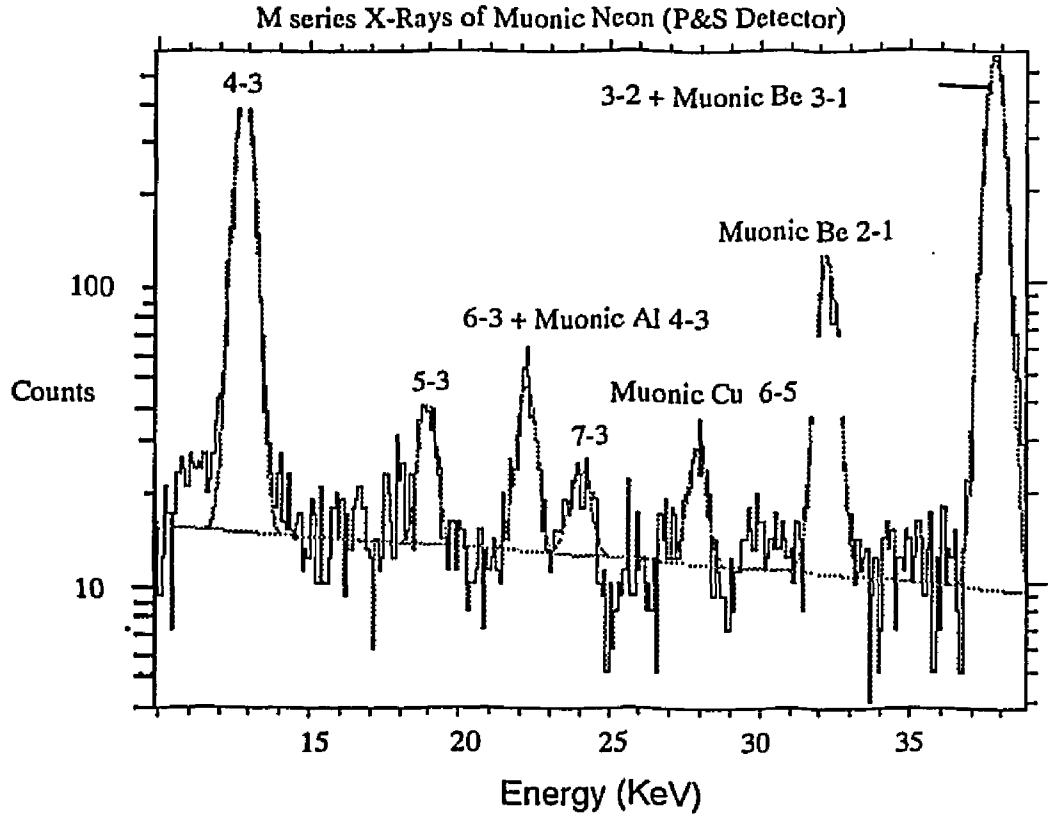

Table 4-7
Single Events
Muonic Neon X-rays-P&S Detector 40 Torr

| K-series | Energy(keV) | FWHM(keV) | Area |
|---|---|---|---|
| 2-1 | 207.218±.009 | .93±.02 | 2024±46 |
| 3-1 | 246.18±.05 | .9±.1 | 133±14 |
| 4-1 | 259.5±.1 | .9±.2 | 33±10 |
| 5-1 | 265.9±.2 | .9±.2 | 24±9 |
| 6-1 | 269.5±.9 | .7±.2 | 36±9 |
| 7-1, 8-1..... | 271.7±.1 | .4±.2 | 31±8 |
| ∞-1 | 277.7±.1 | .4±.2 | 15±6 |
| L-series | | | |
| 3-2* | 38.93±.05 | .71±.01 | 4257±69 |
| 4-2** | 52.50±.05 | .65±.09 | 285±45 |
| 5-2 | 58.71±.09 | .8±.2 | 69±17 |
| 6-2 | 63.11±.04 | .35±.03 | 52±11 |
| M-series | | | |
| 4-3 | 13.565±.006 | .72±.01 | 3222±60 |
| 5-3 | 19.77±.03 | .60±.07 | 185±20 |
| 6-3*** | 23.12±.03 | .65±.06 | 233±21 |
| 7-3 | 24.94±.07 | .8±.2 | 95±18 |

* this line overlaps with the 3-1 x-ray from muonic Beryllium

** this line over laps with the μCu 5-4

*** this line overlaps with the 4-3 x-ray from muonic Aluminum

Table 4-8

Other lines -P&S detector 40Torr

| | Energy(keV) | FWHM(keV) | Area |
|---|---|---|---|
| μAl 4-3 | 23.12±.03 | .65±.06 | 233±21 |
| μAl 3-2 | 65.94±.02 | .79±.05 | 393±25 |
| μBe 2-1 | 33.30±.02 | .71±.04 | 821±32 |
| μBe 3-1 | 39.77±.03 | .25±.07 | 75±20 |
| μBe 4-1 | 41.68±.03 | .26±.07 | 41±10 |
| μBe 5-1 | 42.60±.06 | .5±.1 | 50±13 |
| μBe n-1 | 45.18±.07 | .38±.08 | 64±12 |
| $F^{19}$ Gamma | 197.06±.05 | .9±.1 | 149±17 |
| μCu 6-5 | 28.89±.05 | .6±.2 | 113±18 |
| μCu 5-4 | 53.2±.1 | .58±.2 | 111±44 |

A similar fit was made to the energy spectra of the single photon events seen in the W&M detector; the results of this fit are given in Tables 4-9 and 4-10.

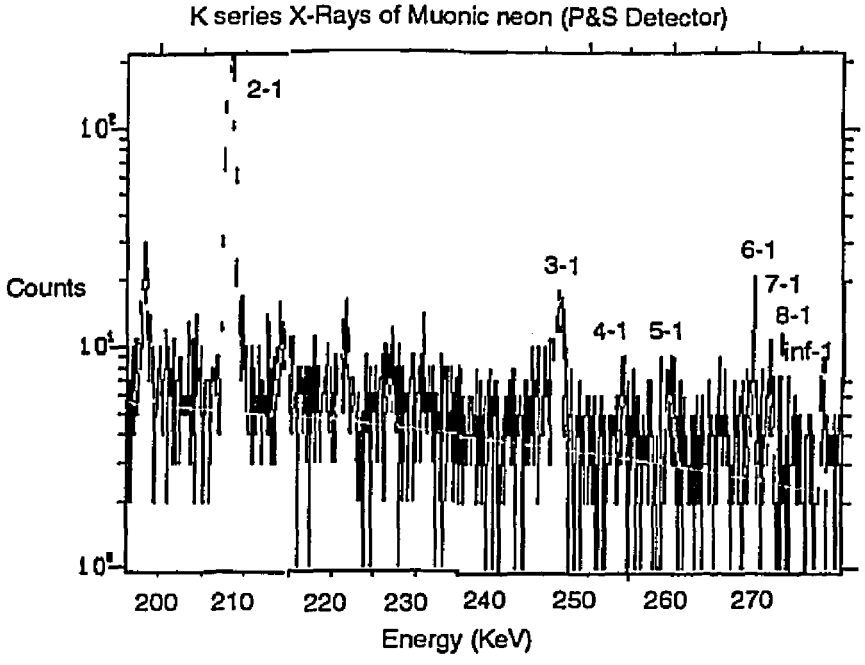
K series X-Rays of Muonic neon (P&S Detector)
2-1
3-1
4-1
5-1
6-1
7-1
8-1
inf-1
Counts
200
210
220
230
240
250
260
270
Energy (KeV)

Fig. 4-5

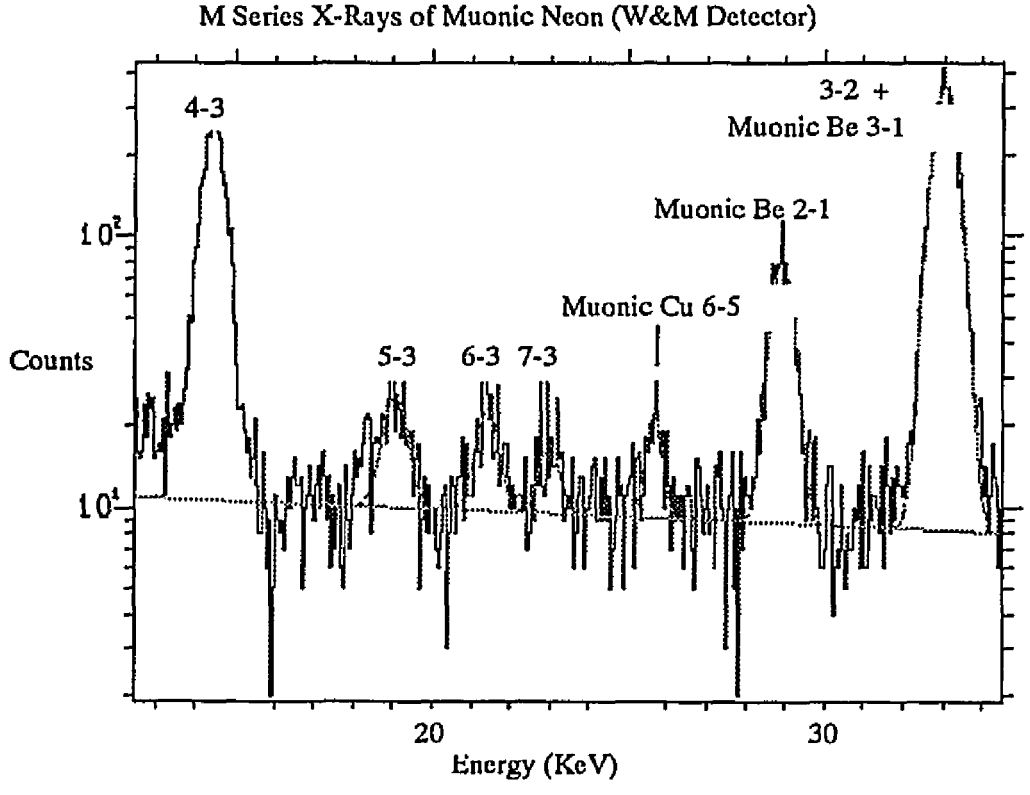
M Series X-Rays of Muonic Neon (W&M Detector)
4-3
3-2 +
Muonic Be 3-1
Muonic Be 2-1
Muonic Cu 6-5
5-3
6-3
7-3
Counts
20
30
Energy (KeV)

Fig. 4-6

Table 4-9
Single Events
Muonic Neon X-rays-W&M Detector 40 Torr

| K-series | Energy(keV) | FWHM(keV) | Area |
|---|---|---|---|
| 2-1 | 207.20±.01 | 1.09±.02 | 1850±45 |
| 3-1 | 246.14±.06 | 1.1±.1 | 127±15 |
| 4-1 | 259.4±.2 | 1±.5 | 19±10 |
| 5-1 | 265.7±.1 | .96±.4 | 26±9 |
| 6-1 | 269.08±.02 | .12±.04 | 15±5 |
| 7-1, 8-1..... | 270.6±.1 | 1.8±.8 | 32±13 |
| ∞-1 | 277.28±.04 | .16±.09 | 8±4 |
| L-series | | | |
| 3-2* | 38.98±.01 | .92±.04 | 4538±665 |
| 4-2** | 52.64±.03 | 1.22±.08 | 316±225 |
| 5-2 | 58.69±.09 | .9±.2 | 90±21 |
| 6-2 | 62.06±.07 | .6±.2 | 55±15 |
| M-series | | | |
| 4-3 | 13.627±.007 | .94±.01 | 3266±61 |
| 5-3 | 19.83±.05 | 1.1±.1 | 231±26 |
| 6-3*** | 23.18±.05 | .9±.1 | 167±23 |
| 7-3 | 25.32±.08 | .8±.1 | 85±19 |

* this line overlaps with the 3-1 x-ray from muonic Beryllium

** this line over laps with the μCu 5-4

*** this line overlaps with the 4-3 x-ray from muonic Aluminum

Table 4-10

Other lines -W&M detector 40Torr

| | Energy(keV) | FWHM(keV) | Area |
|---|---|---|---|
| μAl 4-3 | 23.18±.03 | .9±.1 | 167±22 |
| μAl 3-2 | 65.89±.05 | 1.0±.1 | 240±25 |
| μBe 2-1 | 33.39±.02 | .89±.03 | 920±35 |
| μBe 3-1 | 39.5±.7 | 1.4±.05 | 452±694 |
| μBe 4-1 | 41.68±.03 | .26±.07 | 41±13 |
| μBe 5-1 | 42.23±.09 | 1.1±.2 | 78±25 |
| μBe n-1 | 45.22±.06 | .7±.1 | 93±18 |
| $F^{19}$ Gamma | 196.9±.1 | 1.6±.2 | 132±18 |
| μCu 6-5 | 28.96±.04 | .6±.1 | 109±17 |
| μCu 5-4 | 53.1±.5 | 1.9±..8 | 278±207 |

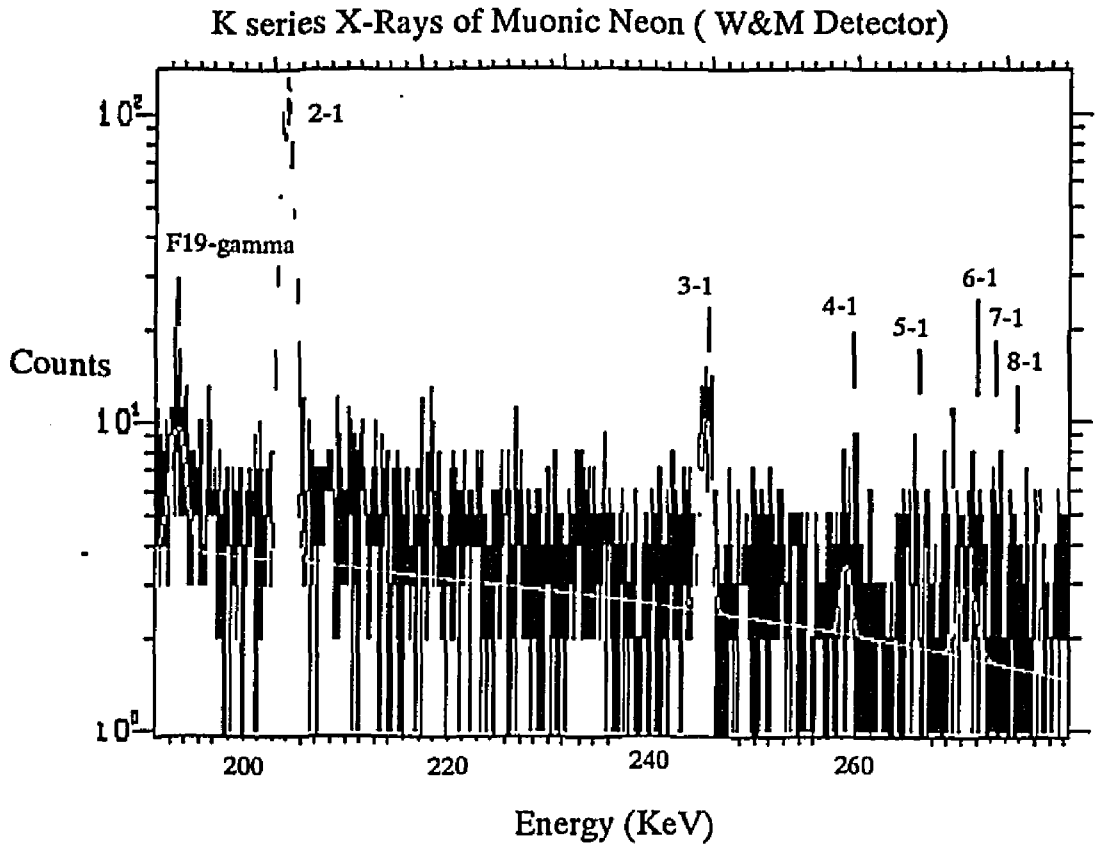


Fig. 4-7

Using the intensities of the K series x-rays given in Tables 4-7 and 4-9 and equation 2.16 in chapter 2, it is now possible to estimate the relative population of the 2S-state. The first step is to calculate the relative intensities of each of the resolved n→1 transitions to the total of all K-series x-rays. Two examples are given below using the notation from chapter 2 :

$$Y(2p\text{-}1S) = K_\alpha/K_{tot} = 1/\,[1+ (K_\beta/K_\alpha) + (K_{>\beta}/K_\alpha)] \qquad (4.2)$$

$$Y(3p\text{-}1S) = K_\beta/K_{tot} = (K_\beta/K_\alpha)/\,[1+ (K_\beta/K_\alpha) + (K_{>\beta}/K_\alpha)]. \qquad (4.3)$$

Table 4-11 lists the calculated relative intensities for both the P&S and the W&M detectors after correcting for the variations in photopeak efficiencies as a function of energy.

Table 4-11
Relative Intensities of the Lyman series of Muonic Neon

| P&S | W&M |
|---|---|
| $K_{tot}$= 5730 ± 134 | $K_{tot}$= 5162 ± 145 |
| $K\alpha/K_{tot}$ = .85 ± .05 | $K\alpha/K_{tot}$ = .86 ± .05 |
| $K\beta/K_{tot}$ = .07 ± .02 | $K\beta/K_{tot}$ = .074 ± .02 |
| $K\gamma/K_{tot}$ = .019 ± .007 | $K\gamma/K_{tot}$ = .012 ± .006 |
| $K\delta/K_{tot}$ = .014 ± .005 | $K\delta/K_{tot}$ = .017 ± .009 |
| $K\varepsilon/K_{tot}$ = .021± .005 | $K\varepsilon/K_{tot}$ = .010 ± .003 |
| $K\zeta/K_{tot}$ = .018 ± .005 | $K\zeta/K_{tot}$ = .020 ± .008 |
| $K_{\infty}/K_{tot}$ = .009 ± .003 | $K_{\infty}/K_{tot}$ = .005 ± .002 |

Substituting these values for Y(np-1S) into expression 2.16 along with the appropriate value of $F_n$ taken from Table 2-2, we find the relative population of the 2S-state of muonic neon at 40 Torr of pressure to be $\varepsilon_{2s}$ = 1.8% ± .2%for the P&S detector and $\varepsilon_{2s}$=1.7%± .2% for the W&M detector. The results of this calculation are consistent with the expectation that something on the order of a few percent of the muons in the cascade reach the 2S-state.

## F. ANALYSIS OF TWO PHOTON EVENTS AT 40 TORR

The coincidence data were collected and saved in twenty one event files. Initially the data were recorded and sorted on-line into 11 different histograms; two histograms were 8192 channel plots of the individual detector energy spectra for events coincident in both detectors, and two 8192 channel histograms of the TAC time distributions of each detector for events coincident in both detectors. The remaining four histograms were identical to the histograms above, except that they were plotted with an 8 bit 256 channel resolution, instead of the 13 bit/8912 channel resolution. With the energy and time spectra reduced to 256 channels three 256 X 256 channel 2-D histograms could be made. Two of these plots were energy vs. time histograms, where the energy of an event is plotted on one axis and the time of the event is plotted on the other axis. There was one of these plots for each detector. The third 2-D histogram plotted the coincident events in terms of energy vs. energy, with the energy deposited in the W&M detector being the X-axis and the energy deposited in the P&S detector being the y-axis. From the Kmax scripting language and the information contained in these plots, a replay instrument was written that would produce energy calibrated and time slew corrected histograms. The data were then replayed with this instrument and resorted into the 11 histograms plus two new ones: Esum, Ediff.

$E_{sum}=(E_{W\&M}+E_{P\&S})$ and $E_{diff}=(E_{W\&M} - E_{P\&S} + \text{constant})$ For a given Esum.

The Ediff and Esum spectra were the most useful energy histograms in the analysis of the two photon events where $E_{W\&M}$ and $E_{P\&S}$ refer to the energies of the photons detected in the W&M and P&S detectors respectively. The Esum histogram is self explanatory; it is simply the sum of the energies of the photons that were detected in coincidence. The Ediff histogram is a plot of the difference in energy of two photons whose energy sum is between two predefined values selected by the user. The constant was also user defined, but only served as a convenience for the plotting of the histogram. The software for the replay instrument was written such that in addition to the six recorded parameters there were seven calculated parameters. These seven created parameters were: 'Ewm' and 'Eps'; which were the energy calibrated responses of each detector calculated in the replay instrument using equations given in Table 4-4 for 40 Torr of pressure; 'Esum', which was the sum of 'Ewm' and 'Eps'; 'Iflag' was an integer parameter which signaled if 'Esum' was between two values defined by the user; 'Ediff', which was the difference between 'Ewm' and 'Eps' for a given 'Iflag'; and the 'STDCwm' and 'STDCps', which were the slew corrected TDC times calculated in the replay instrument using the equations given in table 4-8 for 40 Torr of pressure.

## G. TIME CUTS OF TWO-PHOTON EVENTS

After correcting for time slewing using the methods described early in this chapter, time cuts were placed so as to discard those events that had unrealistic time information. Many of these invalid

events were "zeros"-- i.e. lying along both the time and energy axes (E=0, T=0). These zeros are generated when there is a signal in the energy ADC but not in the time ADC or the reverse. The zeros are not true events and need to be excluded from the analysis.

## H. BACKGROUND

The events that appear on the E vs. E plot, figure 4-8 , can be subdivided into three categories: 1) random coincidences, 2) coincidence summing, and 3) Compton scattering. Random coincidences result from a single photon, or noise pulse in the electronics, being in coincidence with a random noise pulse, or a photon. The time and energy structure of these two photon events is such that they appear as the uniform background or "grass" in the E vs. E plot. The second type of event, coincidence summing, is the result of a photon from the muonic cascade of neon (or any target chamber material) being in coincidence with a random noise pulse or another photon from a muonic cascade. These two photon events form the lines or bands that cross the E vs. E plot and intersect the axis at the energy of a known transition. Compton scattering, the third source of signal, occurs when a single photon Compton scatters in one detector, depositing some fraction of its energy while the scattered photon traverses the target chamber and stops in the second detector. This type of event is the most difficult to distinguish from a true two photon event, for it would generate an event with a time structure and summed energy indistinguishable

from that of a two-photon decay of the 2S-state. These Compton scattered background events form the diagonal features that appear on the E vs. E plot and intersect the ordinate and abscissa at the full energy value of the X-ray that is being scattered.

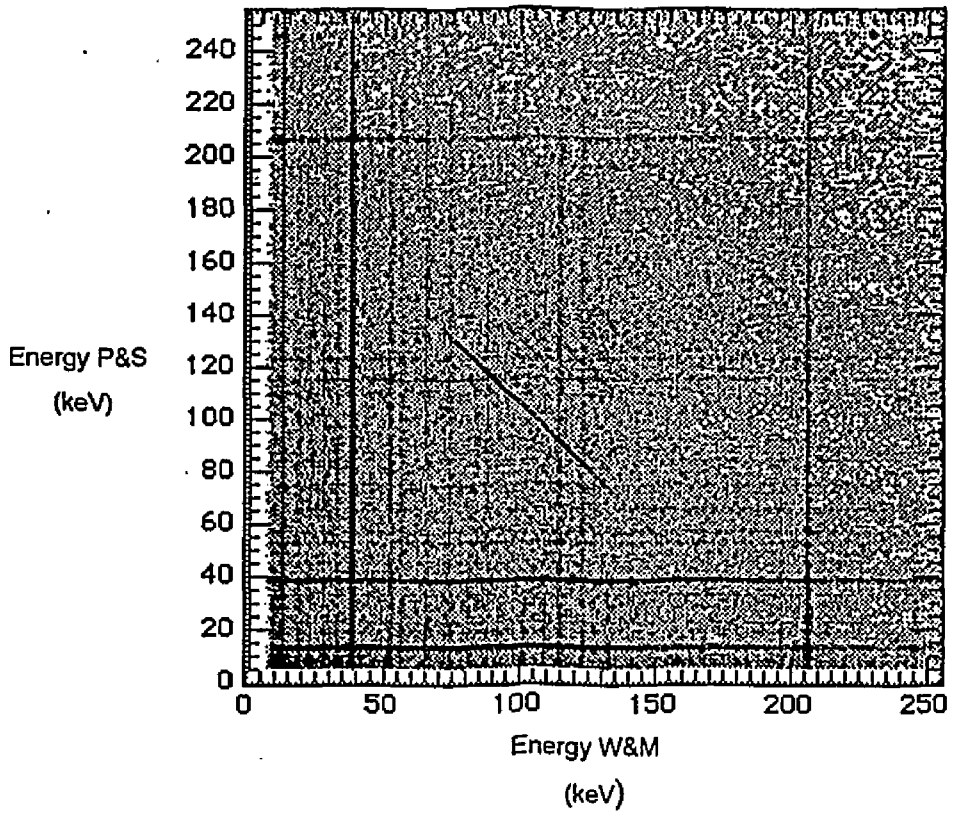


Fig. 4-8, E vs E 40 Torr

Figure 4-8 is an E vs. E plot for two photon events observed in neon at 40 Torr of pressure. The x-axis is the energy that the event deposited in the W&M detector, and the y-axis is the energy deposited in the P&S detector. The units of both axis are in keV. While this Compton scattered background lies on the same 45° line that corresponds to true two-photon decays, the Compton scattering

is kinematically limited; there is a central teardrop-shaped region in the E vs. E plot that is free of Compton scattered events[26]. This Compton free region can be seen in figure 4-8 as the gap in the prominent dark diagonal line that is the $K_\alpha$ sum line of muonic neon ($E_{wm} + E_{ps}$ = 207.228 keV ± 1 keV ); Figure App.-1 in the appendix is a plot that shows the entire Compton free region of the E vs. E plot.

## I. ENERGY CUTS ON THE E VS E SCATTER PLOT

Three energy cuts were made to the E vs. E plot shown in figure 4-8. The first cut was for all coincident events that had an energy sum ( Ewm+Eps = Esum ) between 206 and 208 keV. These events were then sorted as to their energy difference (Ewm - Eps = Ediff) and plotted as an Ediff histogram. This histogram is the diagonal line that corresponds to the $K_\alpha$ sum line as viewed from the origin of the E vs. E plot, see figure 4-10. The two other cuts were similar in nature to the first but were placed on either side of the first cut: 203keV < Esum < 205keV and 209keV < Esum < 211keV. These cuts do not correspond to an observed transition but were made in order to estimate the random background that lies under the cut centered on 207 keV. The background was determined by averaging the counts in the two "side" cuts for the region of interest Fig. 4-10, 4-9, and 4-11 are the respective figures.

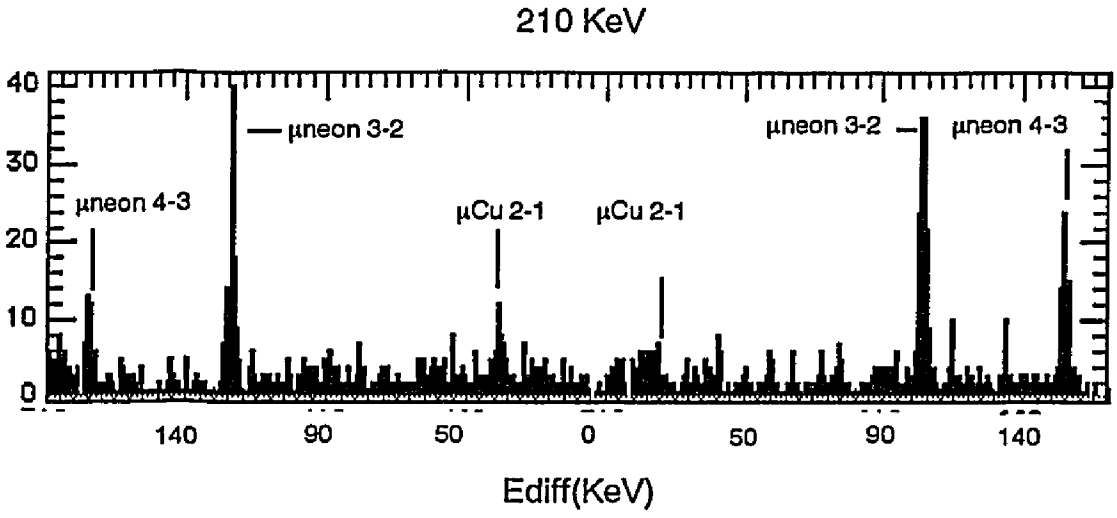


Fig. 4-9

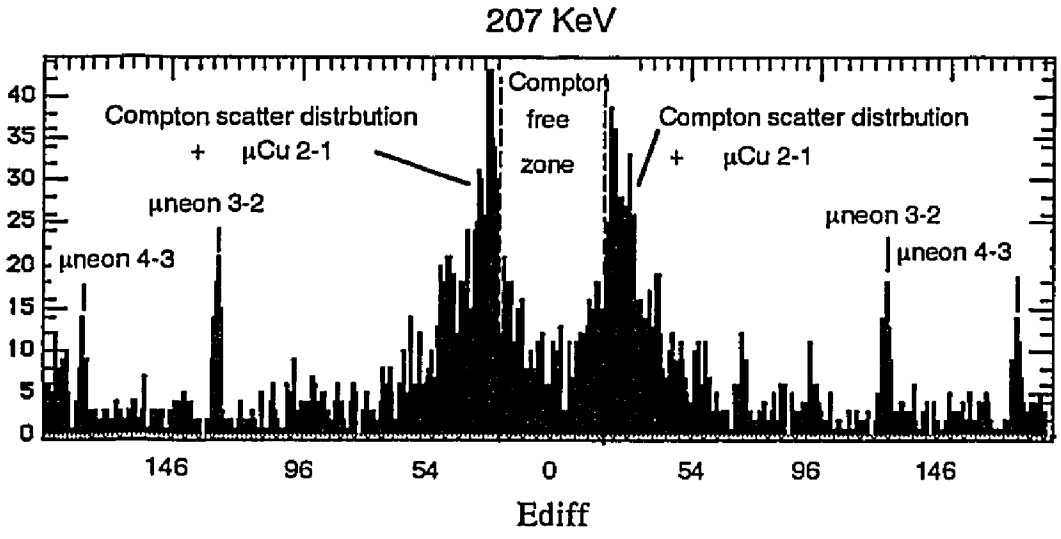


Fig. 4-10

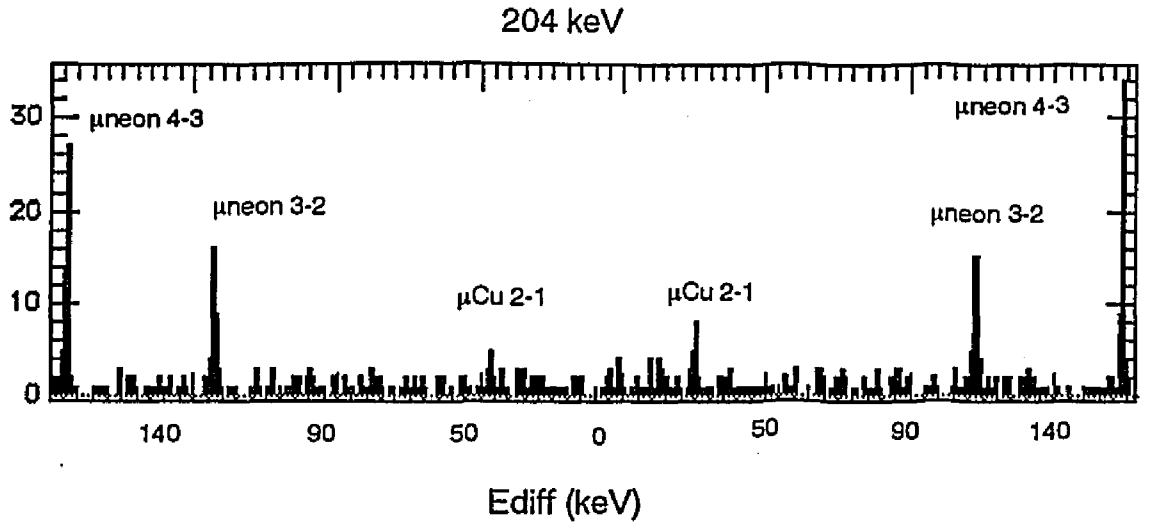


Fig. 4-11

In looking at figure 4-10 one can see that the two large peaks of the Compton distribution extend somewhat into the calculated Compton free region; this is a result of multiple Compton scatters and finite detector resolution. To differentiate these effects from the observed two photon events, three successively narrower (Ediff= ±20, ±10, ±5 ) keV regions about the value Ediff=0 were taken as the Compton free zones. The number of events in each of these zones as well as the estimated average random background are given in table 4-12.

Table 4-12

Number Of Observed 207 keV Two-Photon Events At 40 Torr

| Ediff(keV) | Counts | Background | Counts-Background |
|---|---|---|---|
| ±12 | 230 ± 15 | 96 ± 12 | 134 ± 19 |
| ±10 | 177 ± 13 | 55 ± 9 | 122 ± 16 |
| ±5 | 94 ± 10 | 31 ± 8 | 63 ± 13 |

The number of Compton events that exist on either side of the "gap" is also needed in order to compare the results at 40 Torr with the results of the coincidence at 400 Torr. The data sets for the 40 and 400 Torr conditions were not the same size, making it necessary to compare the ratio of two-photon events to Compton events and not the raw number of events. For this purpose we used the number of Compton events that lie in the region between 20 <Ediff< 75 in the 207 keV histogram, with the average random background determined from the same region in the 204 and 210 keV histograms. The number of Compton events found in this region was 1027 ± 48. The ratio of two-photon events to Comptons is then given in Table 4-13.

Table 4-13

| Ediff(keV) | 2 gamma events/Compton events |
|---|---|
| ±12 | .130 ± .022 |
| ±10 | .119 ± . 035 |
| ±5 | .061 ± .014 |

## J. ANALYSIS OF TWO PHOTON EVENTS AT 400 TORR

The coincidence data at 400 Torr of neon was collected and saved in ten event files titled Neon400%0-%10. The motivation behind doing the coincidence experiment at an increased pressure (400 Torr) was that at the higher pressure electron refilling would destroy the metastability of the 2S-state and that coincidence data collected at 400 Torr would show little or no two photon events,

collected at 400 Torr would show little or no two photon events, thereby providing a control or test with which to confirm that what had been observed at 40 Torr was an actual effect. The analysis of the coincidence data at 400 Torr was done exactly as was the case for the data at 40 Torr. The replay instrument was identical to that of the 40 Torr replay except for changes in the calibration, time slew correction, and additional Ediff cuts at 197 keV, the position of the fluorine 19 nuclear gamma ray.

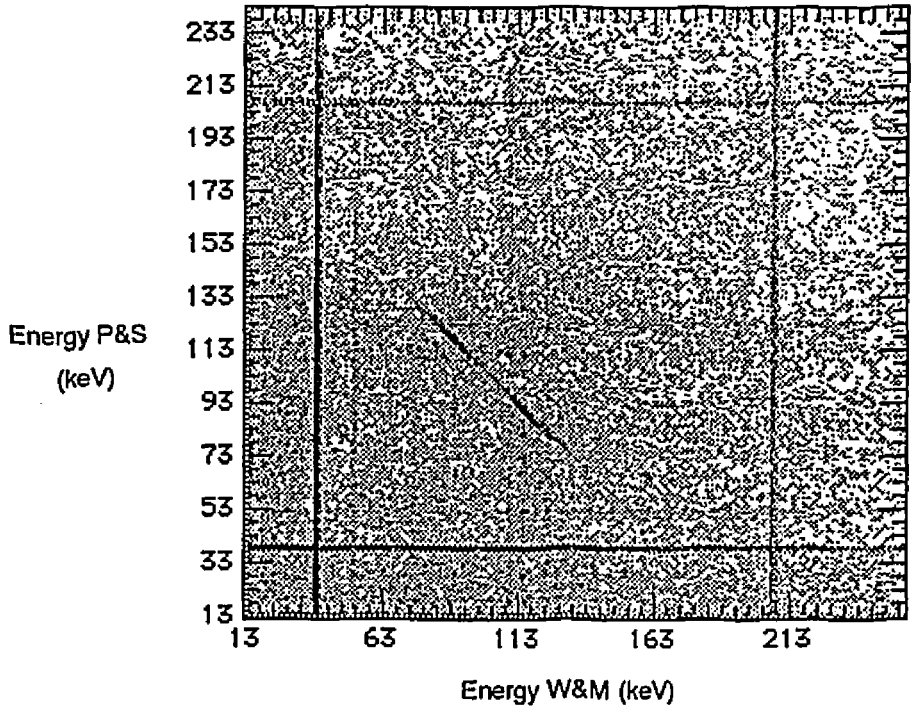


Fig. 4-12 E vs E 400 Torr

Figure 4-12 shows the E vs. E plot for coincident events at 400 Torr of neon in units of keV. With the 400 Torr data calibrated, slew corrected and zeros rejected, six Ediff cuts were made from the E

vs. E plot. One cut was centered on the 207 keV line of the muonic neon Kα line, with its two associated background cuts to either side centered at 204 and 209 keV, as in the 40 Torr case. In addition there were cuts of equal width placed at 197 keV corresponding to the nuclear gamma of $F_{19}$ which is the result of muon capture on the neon nucleus, and two background cuts centered at 194 and 200 keV. The reason for including the 197 keV transition in this analysis is that the line shows the effects of Compton scattering between the detectors, and the transition is not expected to have any significant two-photon component. Considering these properties the 197 keV line can serve as a measure of the amount of Compton scattering that takes place between detectors.

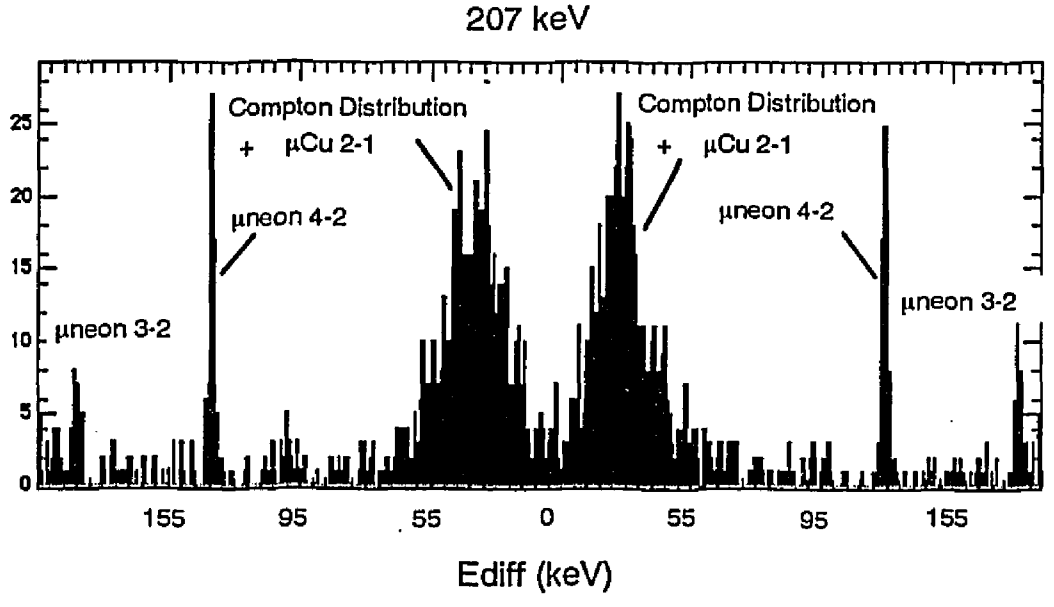


Fig. 4-13

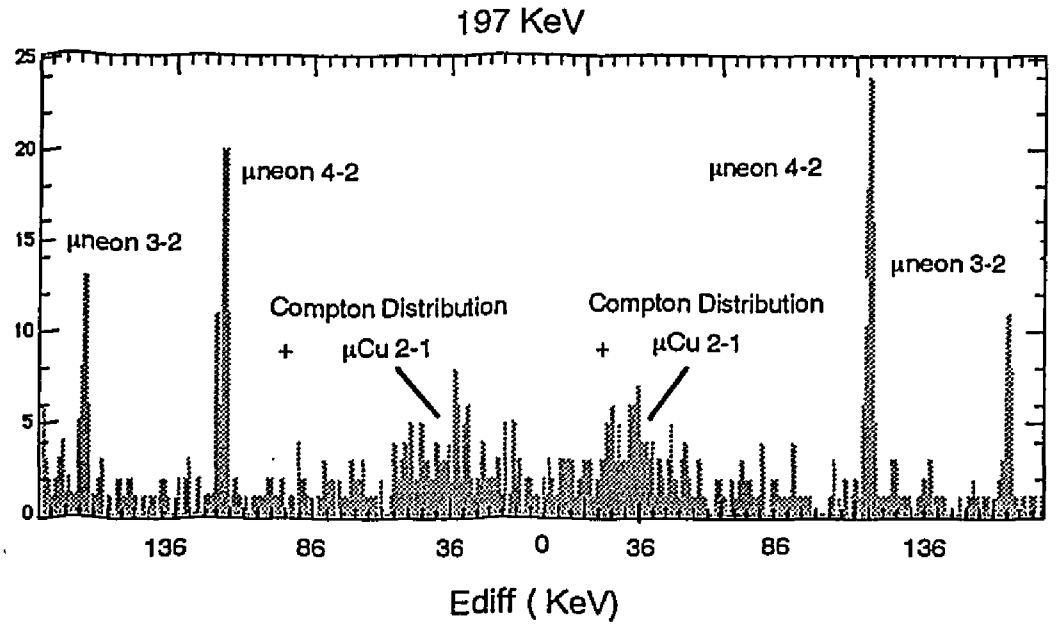


Fig. 4-14

The background cuts associated with these histograms can be found in the Appendix. Tables 4-14 and 4-15 present the counts and average background for the Kα sum line and the $F^{19}$ gamma ray in the regions Ediff=±12, ±10, ±5 keV at 400 Torr of neon.

Table 4-14

Number of Observed 207 keV Two Photon Events At 400 Torr

| Ediff | Events | Background | Counts-Back. |
|---|---|---|---|
| ±12 | 136 ± 12 | 28 ± 7 | 108 ± 14 |
| ±10 | 96 ± 12 | 25 ± 7 | 69 ± 12 |
| ±5 | 44 ± 7 | 10 ± 4 | 34 ± 8 |

Table 4-15

Number of Observed 197 keV Two Photon Events At 400 Torr

| Ediff(keV) | Events | Background | Counts-Background |
|---|---|---|---|
| ±12 | 42 ± 6 | 23 ± 7 | 19 ± 9 |
| ±10 | 32 ± 6 | 19 ± 6 | 13 ± 8 |
| ±5 | 15 ± 4 | 11 ± 4 | 4 ± 6 |

For the Kα sum line the number of Compton events that lie in the 20< Ediff < 70 keV regions was found to be 818 ± 35, while the Compton events in a similar region along the 197 keV sum line was 144 ± 20. The ratio of two-gamma events to Compton events for the 207 and 197 keV lines at 400 Torr of neon is given below in table 4-16.

Table 4-16

Ratio of 2 Gamma events to Compton events at 400 Torr Neon

| Ediff(keV) | 207 keV | 197 keV |
|---|---|---|
| ±12 | .132 ± .018 | .132 ±.065 |
| ±10 | .084 ± .015 | .090 ± .057 |
| ±5 | .041 ± .010 | .027 ± .041 |

Before the Compton scattering at 197 keV can be used to model Compton scattering at 207 keV one final correction needs to be made. For a given energy the limit of the Compton-free zone is determined by the events that undergo 180° Compton scattering. At 207 keV this corresponds to 92.6 keV being deposited in the first detector, while the secondary photon of 114.3 keV is completely

absorbed in the second detector. This generates a coincident event with Ediff=21.7 keV, producing a Compton free gap about 43 keV wide. At 197 keV a 180° scatter produces a coincident event with an Ediff= 25.5 keV and a "gap" about 51 keV wide. This results in the 197 keV data being distributed over about 15% more area, reducing the number of counts seen per channel. Only after correcting for this fact can the 207 and 197 keV data be compared.

Table 4-17

Corrected 2 Gamma to Compton Ratios (197 keV)

| Ediff(keV) | 197 keV |
|---|---|
| ±12 | .156 ± .077 |
| ±10 | .106 ± .068 |
| ±5 | .032 ± .049 |

The ratios in Table 4-17 now represent an estimate of the amount of Compton scattering present as a background in each of the various Ediff regions at an energy of 207 keV. This background can then be subtracted from the number of events seen in the Compton "gap" at 207 keV for both the 40 and 400 Torr of neon conditions. Table 4-21 presents the final results of subtracting this calculated background from the information given in tables 4-16 and 4-19, and the number of observed 2S-state two photon decays.

Table 4-18

Ratio of 2 Gamma Events to Compton Events with Compton Background Subtracted

| 40 Torr Ediff(keV) | Ratio 2γ/ Compton | 2S two Photon decays |
|---|---|---|
| ±12 | -.026± .080 | -26 ± 82 |
| ±10 | .013 ± .076 | 13 ± 78 |
| ±5 | .029 ± .051 | 30 ± 52 |
| 400 Torr Ediff(keV) | Ratio 2γ/ Compton | 2S two Photon decays |
| ±12 | -.024 ± .078 | -20 ± 64 |
| ±10 | -.022 ± .070 | -18 ± 57 |
| ±5 | .009 ± .050 | 7 ± 41 |

The large errors in these results reflect the statistics associated with the 197 keV nuclear gamma ray. It is also worth noting that the time structure of the events in the Compton free gap (two photon events from the 2S-state) was not significantly different from the time structure of other non-2S two photon events.

## K. PREDICTED FRACTION OF TWO PHOTON DECAYS

An estimate of the population of 2S-states can be obtained with a simple calculation. The Kβ sum peak in the Esum histograms for both the 40 and 400 Torr data is the result of a Kα•Lα coincidence. The number of these observed coincidences is a function of detector efficiency denoted Eff<KL>, and the fractional yield of both the Kα and Lα transitions denoted here as $K_{tot}/K\alpha$ and $L_{tot}/L\alpha$. With this information and the knowledge of the number of observed Kα•Lα

coincidences, $N_{KL}$, one can write an expression for the number of muonic neon atoms expected to be formed in the target chamber

$$N_{\mu neon} = N_{KL} \cdot (K_{tot}/K\alpha) \cdot (L_{tot}/L\alpha) \cdot (Eff<KL>). \qquad (4\text{-}2)$$

To determine the number of 2S two-photon events that one would expect to find in the ± 5 keV gap in the Ediff histograms, one multiplies expression 4-2 by the relative population of the 2S-state, $\varepsilon_{2s}$, as determined from the singles spectra. One also needs to account for the angular correlation between the two photons of a 2S decay, 3/4 $(1+ \cos^2\theta)$, detector efficiency, $Eff<\gamma\gamma>$, and the fraction of the entire 2 photon spectrum represented in the ± 5 keV gap, $F_{EDIFF\ CUT}$. The final expression for the number of 2S states predicted to be populated can be written

$$N_{2S} = N_{KL} \cdot \frac{K_{tot}}{K\alpha} \cdot \frac{L_{tot}}{L\alpha} \cdot \frac{Eff<\gamma\gamma>}{Eff<KL>} \cdot \varepsilon_{2s} \cdot 3/4\,(1+\cos^2\theta) \cdot F_{EDIFF\ CUT} \qquad (4\text{-}3)$$

At 40 Torr of pressure $N_{KL}$ was found to contain 7921± 89 counts, The $K_{tot}/K\alpha$ and $L_{tot}/L\alpha$ fractional yields were determined after a least-squares fits were performed on the single detector energy histograms. The values are found to be $K_{tot}/K\alpha$ =1.06 ± .01 and $L_{tot}/L\alpha$ = 1.027 ± .01. The ratio of detection efficiencies was estimated by taking the value of $Eff<\gamma\gamma>$ at the midpoint of the two photon spectrum, $E_{\gamma 1} = E_{\gamma 2}$ = 104 keV, so that $Eff<\gamma\gamma>/Eff<KL>$ = 1.94 ± .09. The value for $\varepsilon_{2s}$ 1.8% ± .2% was taken from the calculations in section 4E, and the angular correlation factor evaluates to a factor of 1.5. The fraction of the two photon spectrum that corresponds to

±5 keV was estimated by fitting a 4th order polynomial to the two photon spectrum and taking the ratios of the integrated area of ±5 keV region to that of the entire spectrum, ±207 keV. Using this method $F_{EDIFF\ CUT}$ was found to be equal to approximately 3.1% ± .001%. Combining all of these results one find that the predicted number of 2S two photon decays to be found in the ±5 keV gap = 14 ±1. Unfortunately, no singles data were taken at 400 Torr of neon so that $\varepsilon_{2s}$ is undetermined and the above calculation cannot be performed for this pressure condition. Table 4-19 lists the observed and predicted number of 2S decays for each of the Ediff regions

Table 4-19

Number of 2γ events after Compton background subtracted (40 Torr )

| Ediff(keV) | % of total 2γ Spectrum | Predicted | Observed |
|---|---|---|---|
| ±12 | 7.5% ± .1% | 33 ± 2 | -26 ± 82 |
| ±10 | 6.2% ± .1% | 28 ± 2 | 13 ± 78 |
| ±5 | 3.1% ± .1% | 14 ± 1 | 30 ± 52 |

With the information in Table 4-19 one can calculate the two-photon decay fraction $N_{2\gamma}$, described in equation 2.18. The two-photon decay fraction is simply the ratio of the observed to the predicted number of possible 2S type states. The decay fraction also provides an estimate of the rate at which modes other than the two photon decay mode depopulate the 2S-state. The decay ratios

predicted from equation 2.23 are .974 at 40 Torr and .277 at 400 Torr. The actual ratios are given below in table 4-20.

Table 4-20

| Ediff(keV) | Decay Ratio (40 Torr) |
|---|---|
| ±12 | -.8 ± 3 |
| ±10 | .5 ± 3 |
| ±5 | 2 ± 4 |

Using the three values given in table 4-20 and the expression for the decay fraction;

$$N_{2\gamma} = \Gamma_{2\gamma} / \Gamma_{2\gamma} + \Gamma_{\text{all other}} \qquad (4.2)$$

where $\Gamma_{2\gamma} = 2 \cdot 10^9$ Sec$^{-1}$. One can solve equation 4.2 for the decay rate $\Gamma_{\text{all other}}$ of all other competing modes present at 40 Torr. One finds $\Gamma_{\text{all other}} \approx -4.5 \cdot 10^9$ Sec$^{-1} \pm 17 \cdot 10^9$ Sec$^{-1}$, $2 \cdot 10^9$ Sec$^{-1} \pm 12 \cdot 10^9$ Sec$^{-1}$ and $-1 \cdot 10^9$ Sec$^{-1} \pm 2 \cdot 10^9$ Sec$^{-1}$, receptively by comparison the decay rates due to electron refilling were expected to be on the order of $10^{10} \cdot P$ (see equation 2.23), which yields to $\approx 5.2 \cdot 10^8$ Sec$^{-1}$ at 40 Torr and $5.2 \cdot 10^{10}$ Sec$^{-1}$at 400 Torr.

# CHAPTER 5

## CONCLUSION

The intent of this experiment was to study the conditions under which 2S formation and metastability might exist in neon gas at room temperature. The observation of the 2S→1S two photon transition would represent direct evidence for the presence of 2S metastability. The analysis of the single photon data taken at 40 Torr revealed that approximately 1.8% of the captured muons populate the 2S-state. The actual search for two photon transitions was carried out in the coincident data taken at 40 Torr and again at 400 Torr. It was conjectured that at the higher pressures electron refilling would inhibit the metastability more than that seen at 40 Torr. Demonstrating a pressure dependence would be positive evidence that one had actually observed 2S-state metastability.

The analysis of the two photon data revealed that, to within the experimental uncertainties, both the 40 and 400 Torr data sets were identical with regard to the number of observed 2S type two photon decays. Further analysis of the 40 Torr coincident data yielded estimates for the total decay rate of all other transitions that compete with the two photon transitions to deplete the 2S population. These "other" rates were of the on the order of $10^9$ $Sec^{-1}$,

which is consistent with the predicted rates for Auger and Ruderman transition. This suggests that at 40 Torr (and 400 Torr) there are electrons present when the muon reaches the 2S-state: This conclusion is inconsistent with ref. 9, where it was stated that all the K and L shell electrons were stripped during the cascade and electron refilling did not take place below 0.5 bar (500 Torr).

The lack of observed two-photon events in the experiment suggests that metastable muonic 2S states may well exits only for $Z < 10$ in gaseous compounds at pressures lower than 40 Torr.

APPENDIX

Table App.-1
Calibration source data

| | | |
|---|---|---|
| CO-57 | Half-life | 271.79 days |
| | Photon energy (keV) | Emission Prob. (%) |
| | 14.41 | 9.14 |
| | 122.06 | 85.68 |
| | 136.47 | 10.67 |
| Am-241 | Half-life | 432.71 years |
| | Photon energy (keV) | Emission Prob. (%) |
| | 26.345 | 2.4 |
| | 59.537 | 35.9 |
| Bi-207 | Half-life | 31.8 years |
| | Photon energy (keV) | Emission Prob. (%) |
| | 569.70 | 97.8 |
| | 1063.66 | 74.9 |
| Ba-133 | Half-life | 31.8 years |
| | Photon energy (keV) | Emission Prob. (%) |
| | 30.97 | 62.0 |
| | 35.2 | 22.2 |
| | 53.16 | 2.20 |
| | 79.61 | 2.63 |

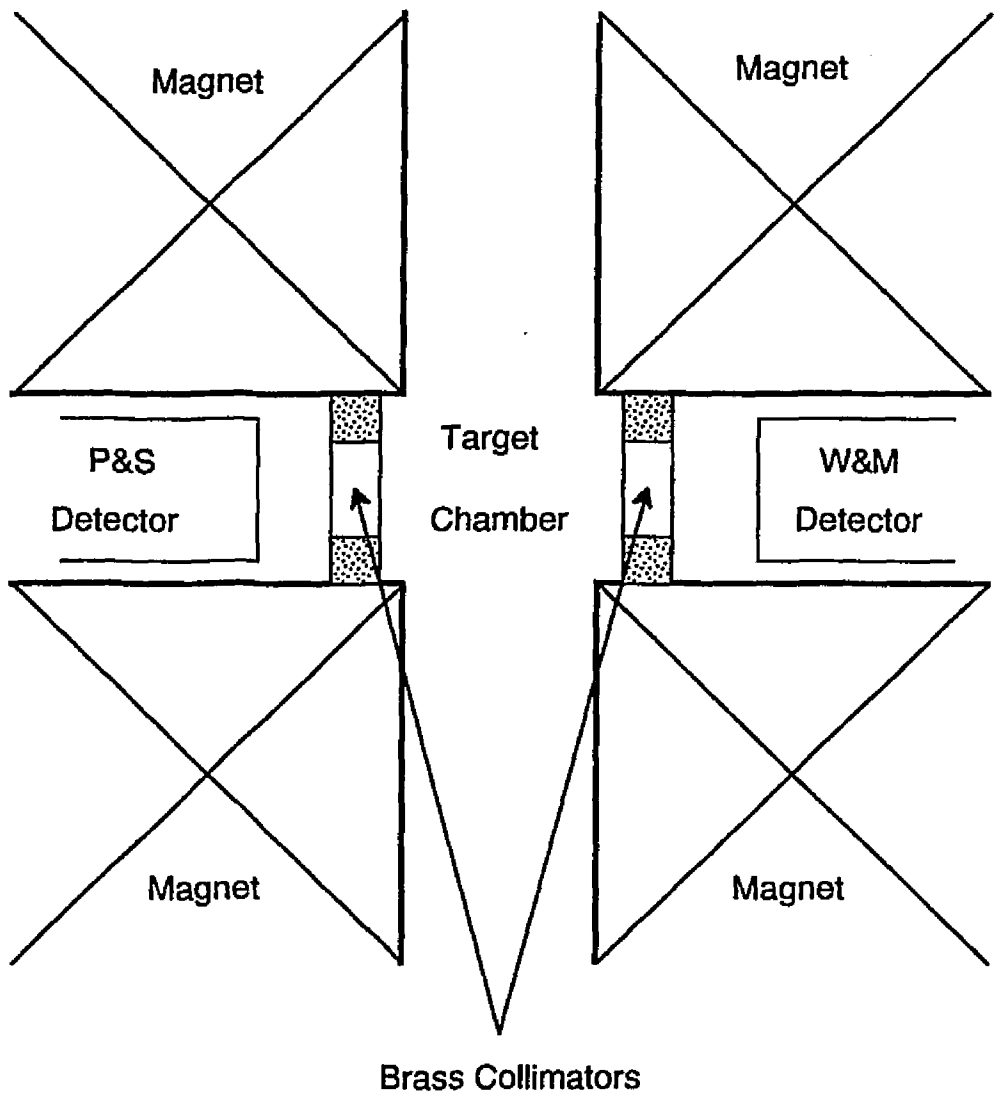


Figure App.-1 Detector Collimation

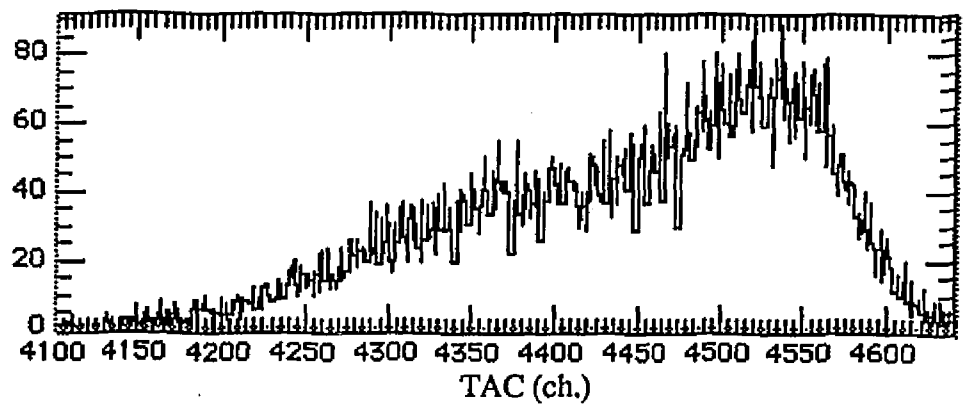


figure App.-2 TAC timing $\mu$neon 3-2 transition

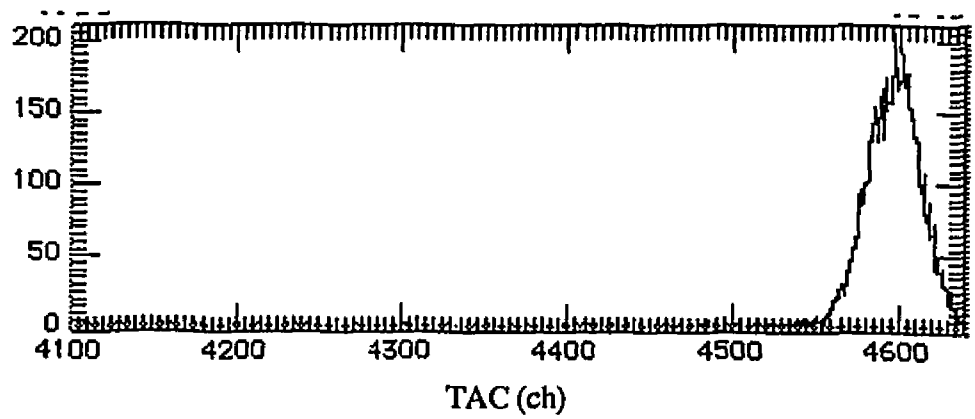


figure App.-3 TAC timing $\mu$neon 2-1 transition

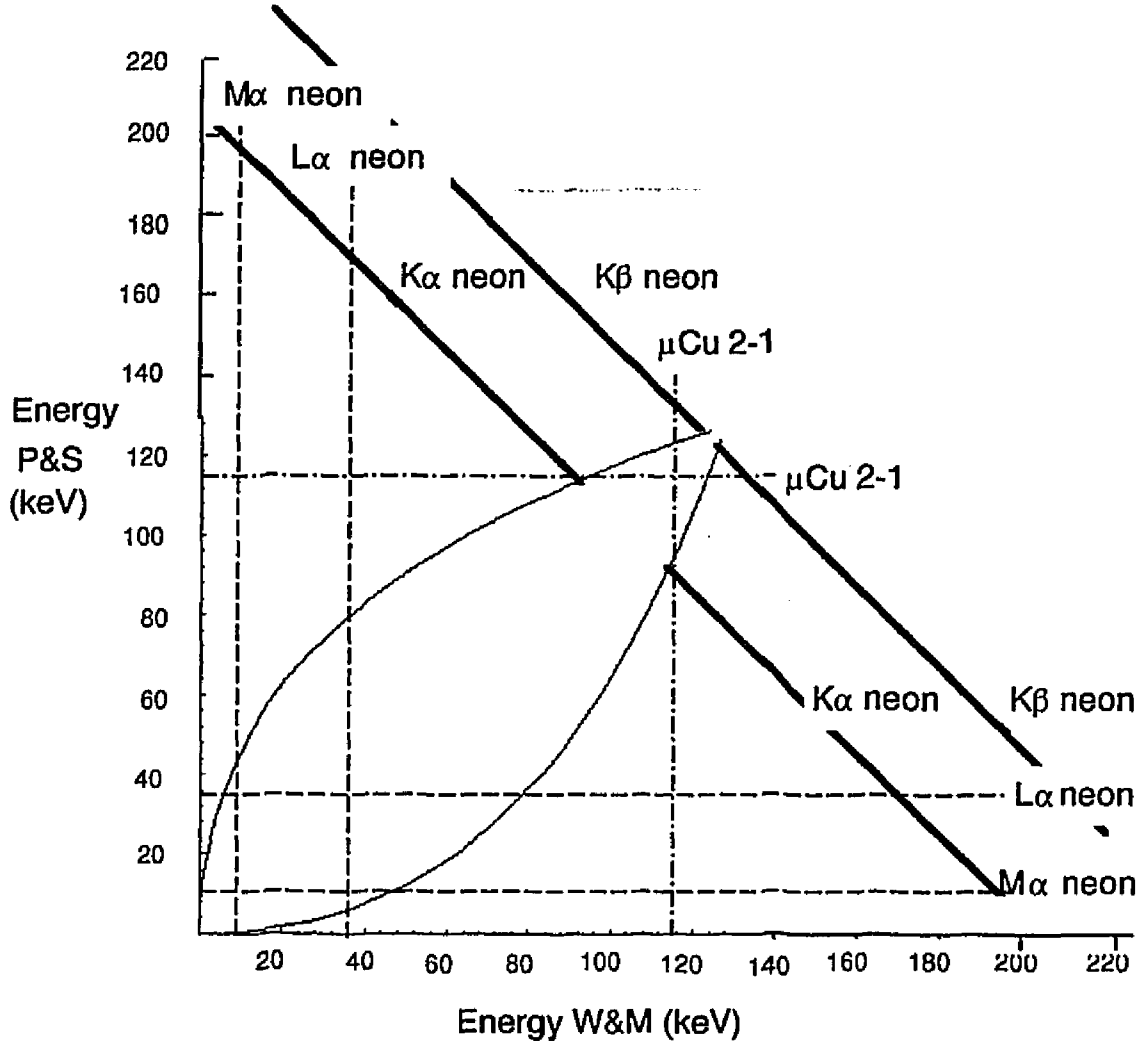


Figure App.-4 Compton free region

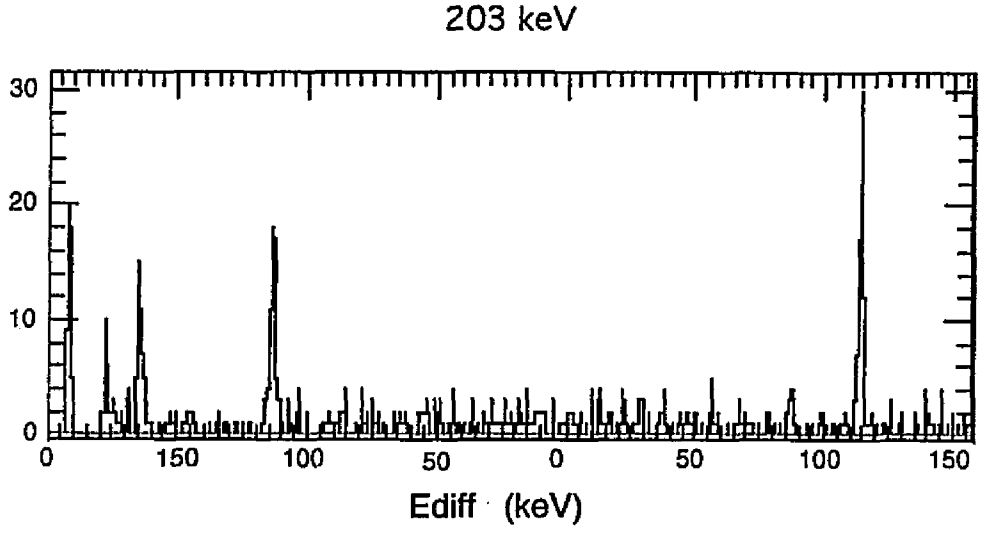


Figure App.-5 Background cut for 197 keV

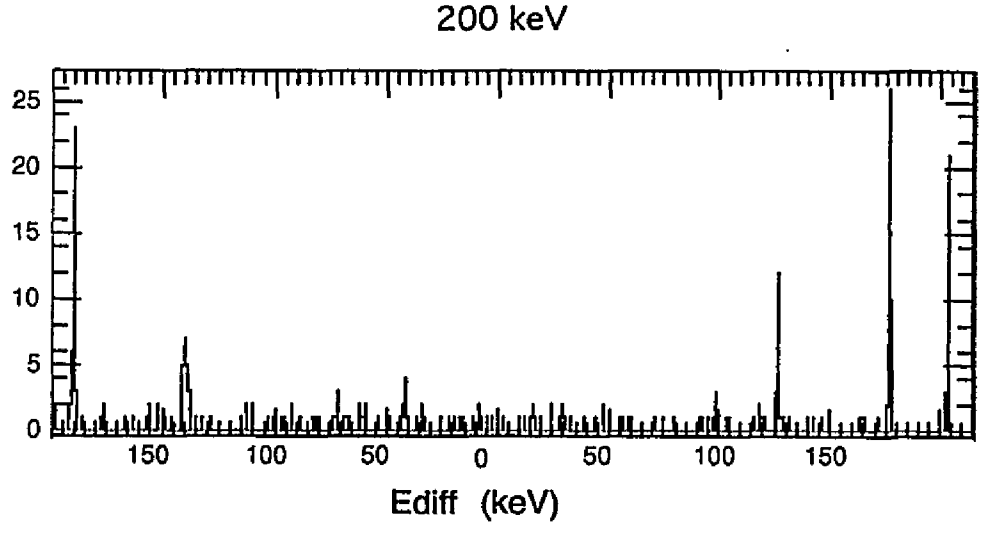


Figure App.-6 Background cut for 197 keV

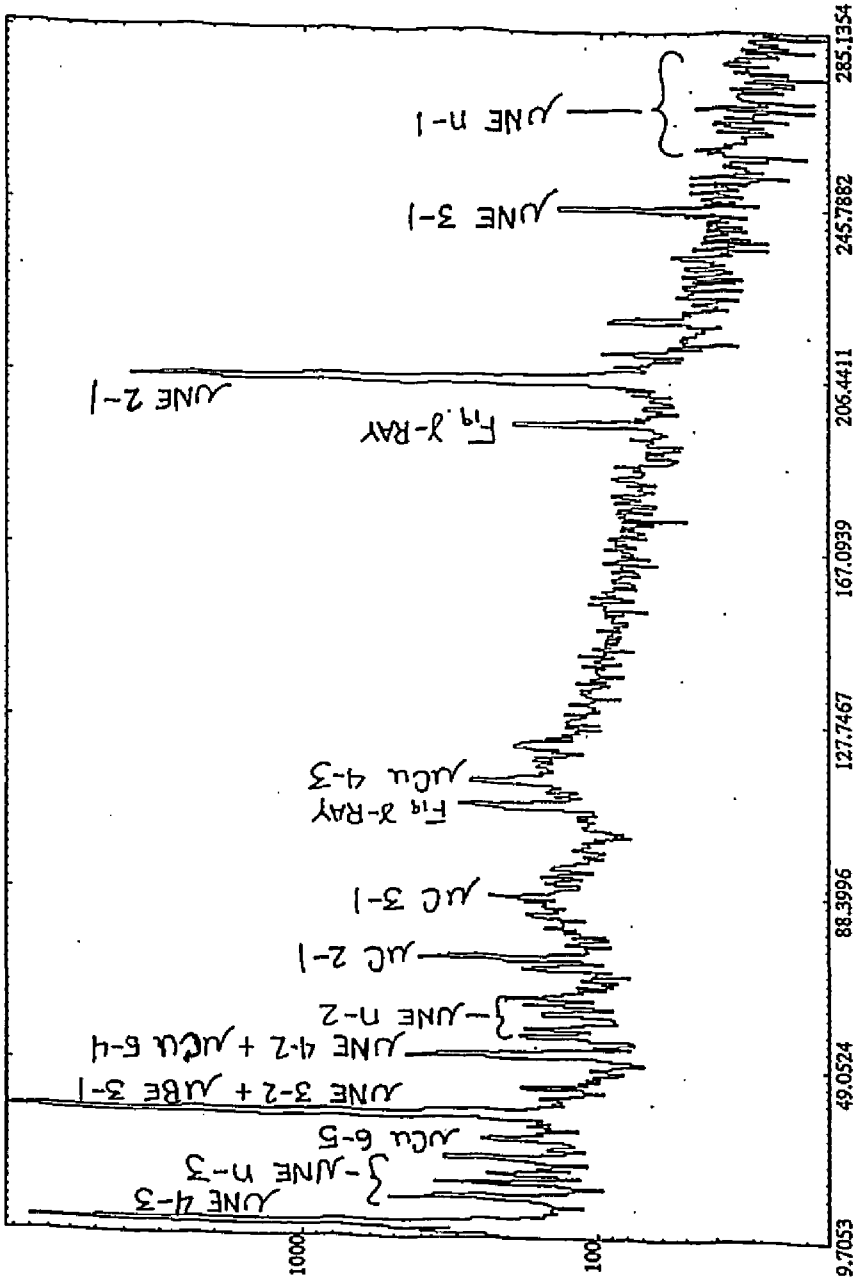


figure App.-7 Energy P&S 400 Torr (keV)

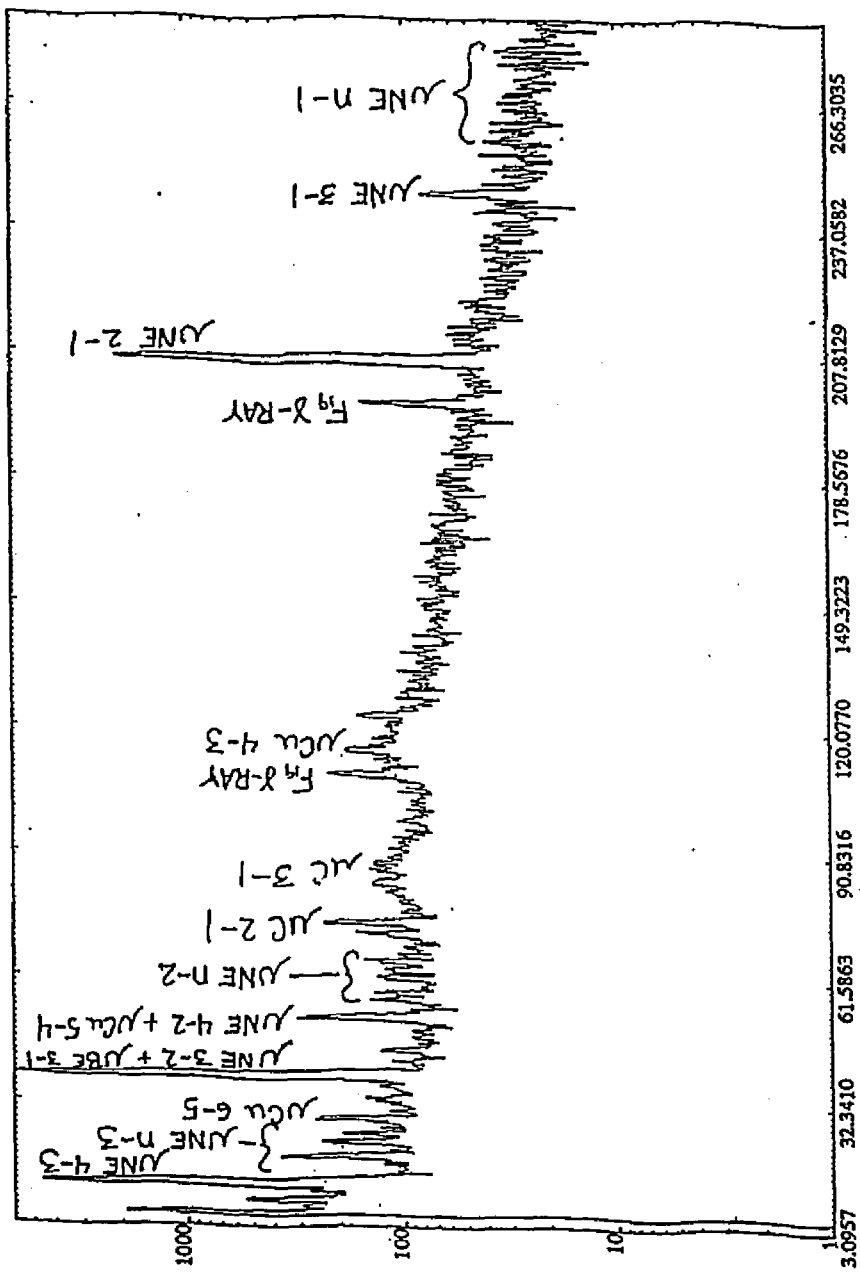


figure App.-8 Energy W&M 400 Torr (keV)

## REFRERENCES


1. Campbell, B. et al, Phys. Lett. 225B, 4, 419 (1989).
2. Korenman, G.Ya. and Rogovaya, S.I., Journal of Physics, B13 641 (1980)
3. David C. Walker, Muon and muonium Chemistry (Cambridge Univ. Press) pg.153 (1983).
4. Bacher et al., Phys. Rev. Lett. 54, 2087 (1985).
5. Horvath, D. and Lambrecht, R., Exotic Atoms, Elsevier, Amsterdam (1984).
6. Carter, A.L. et al., Phys. Rev. Lett. 124B, No. 6, 465 (1983)
7. Feinberg, G. and Chen, M.Y., Phys. Rev. D10, 190 (1974).
8. Klarsfeld, S., Phys. Lett. 30A, 7, 382 (1969).
9. Grechukin, D.P. and Soldatov, A.A., Sov. Phys. JETP 45, 205 (1977).
10. Missimer, J. and Simons, L. , Phys. Rep. 118, No. 4 (1985).
11. Bacher et al., Phys. Rev. A39, 1610 (1989).
12. Ruderman, M., Phys. Rev. 118, No. 6, 1632 (1960).
13. Bertin et al., Nuovo Cimento 26B, 433 (1975).
14. Bethe, H. and Salpeter, E. , Quantum mechanics of one and two electron atoms, Plenum, New York (1977).
15. Ehrhart et al., Phys. Rev. A311, 259 (1983).
16. Zon, B., Raoport, L., JETP Lett. 7, 52 (1968)
17. Drake, G., Phys. Rev. A34, 2871 (1986).

18. Anderhub et al., Phys. Lett. 143B, 65 (1984).

19. DeCecco et al., Hyperfine Int. V76, 275 (1993).

20. Simon, L., Phys. Scripta T22, 90 (1988).

21. Livingood, J., Principles of Cyclic Particle Accelerators, Van Nostrand, New York, (1961).

22. Kmax, SPARROW Coporation, Mississippi State

23. FIT, C.T.A.M. de Laat, Werkgroep Fysische Informatica, Rijiksuniversiteit, Utrecht.

24 Bevington, P., Data Reduction and Error Analysis for the Physical Sciences, McGraw-Hill, NewYork (1969).

25. Seltzer, S., Nuc Instr. and Meth. 188, 133 (1981).

26. Dodson, G.W. , Thesis, The College of William and Mary (1979).

# VITA

While there are many creation myths surrounding his origins, most scholars agree that on the twenty first of January, 1965, in Lyons, New York, Bernhard Wilhelm Bach was spontaneously generated when the fart from a March-born cat blew across a stale Cheerio that had been bonded to a linoleum floor with grape Kool-Aid. His parents dreams had been answered. Raised and educated beneath a fever tree, in 1987 he graduated from the University of Colorado with a Bachelor's degree in physics. In May 1989 he entered graduate school at the College of William and Mary in Virginia and immediately began thinking of ways to get back to Boulder. He completed the requirements for a Doctor of Philosophy degree on June 16, 1995.